Application of the adiabatic compression scenario to the radio relic in the galaxy cluster Abell 3411-3412

Charissa Bronwyn Button
Supervised by Dr Paolo Marchegiani

A dissertation submitted to the Faculty of Science, University of the Witwatersrand, Johannesburg, in fulfilment of the degree Master of Science.

Johannesburg, February 2020

Declaration

I declare that this dissertation is my own, unaided work. It is being submitted for the degree Master of Science at the University of the Witwatersrand, Johannesburg. It has not been submitted before for any degree or examination at any other University.

(Signature of candidate)

18th day of February 2020 at Johannesburg.

Abstract

Radio relics are non-thermal, steep-spectrum ($\alpha < -1$) diffuse radio sources found in the peripheral regions of galaxy clusters. The emission is produced through synchrotron radiation as relativistic electrons ($\gamma \gg 1000$) move in helical paths through the magnetic fields of the intracluster medium (ICM). These electrons have to be (re-)accelerated at the position where the emission is observed since the electron diffusion time over distances greater than 50 kpc from any compact source is longer than their radiative lifetime (~ 0.1 Gyr). Because radio relics have been observed to trace shock fronts, they are widely considered to originate in intracluster shock waves. However, the most widely-used model for describing this (re-)acceleration process at shock fronts, the diffusive shock acceleration (DSA) model, has several challenges, including the fact that it is inefficient at low shock Mach numbers. In light of these challenges, it is worthwhile to consider alternative mechanisms. One possibility is the adiabatic compression by a shock wave of a residual fossil electron population which has been left over from a radio galaxy jet. This project adapts the adiabatic compression model to act on a general electron spectrum. The model is then applied to the relic hosted in the merging galaxy cluster Abell 3411-3412, where a radio bridge between the relic and a radio galaxy has been observed, to try to reproduce the spatial structure of the spectral index of the relic. The results show that the adiabatic compression model can reproduce the observed spectral indices across the relic. Furthermore, the adiabatic compression model appears to be able to reproduce the observed spectra for a shock Mach number that is lower than the value predicted by the DSA-type modelling of this relic and is in accordance with the values derived from X-ray observations. The results also seem to suggest that other mechanisms, such as an expansion phase or post-shock turbulence, affect the spectrum behind the shock front.

Acknowledgements

I would like to thank my supervisor, Dr Paolo Marchegiani, for his support and oversight as I worked on this project. I have learnt so much during my studies and Dr Marchegiani was always available to read and correct the work that I did. I would also like to thank my fellow students who worked in the same office for their support and friendship.

I gratefully acknowledge the South African Radio Astronomy Observatory (SARAO) for funding me throughout my degree.

I am ever grateful to my family for their constant support and encouragement to pursue my studies. My father first sparked my interest in science and I have enjoyed our many conversations about science and about what I have been learning. I am always thankful to my mother for her constant love and support. I am grateful to each of my sisters who have constantly encouraged me and for enjoying with me each milestone that I have achieved. I am grateful to my grandparents who have always been interested in my studies and have constantly supported me in their prayers.

Contents

List of Figures

List of Tables

List of Symbols

c	Speed of light
e	Electron charge
m	Mass of an electron
P_e	Electron momentum
p	Dimensionless momentum of a single electron
P	Pressure
V	Volume
v	Speed
γ	Electron Lorentz factor
N	Electron energy number density or the electron spectrum
s	Electron spectral index, $N(\gamma) \propto \gamma^{-s}$
ν	Frequency
$P_{\rm sync}$	Synchrotron power of a single electron
L_ν	Luminosity
F_ν	Flux density
α	Spectral index, $F_\nu \propto \nu^\alpha$
D_L	Luminosity distance
z	Redshift
B	Magnetic field strength
$u_{\rm B}$	Magnetic field energy density
$u_{\rm C}$	Cosmic microwave background radiation energy density
$\mathcal{M}$	Shock Mach number

List of Abbreviations

AGN	Active Galactic Nucleus
CMB	Cosmic Microwave Background
COBE	Cosmic Background Explorer
CR	Cosmic Ray
DSA	Diffusive Shock Acceleration
GMRT	Giant Metrewave Radio Telescope
ICM	Intracluster medium
LOFAR	Low-Frequency Array
VLA	Very Large Array
WMAP	Wilkinson Microwave Anisotropy Probe

Chapter 1

Introduction

This dissertation focuses on galaxy clusters and the origin of the radio emission known as radio relics. The outline of this chapter is as follows: the next section provides a brief introduction to the current cosmological model and some of the important open questions and briefly describes the importance of radio astronomy. Section 2 describes the properties and formation of galaxy clusters and their diffuse radio emission. Section 3 discusses the problem of the origin of radio relics. Section 4 presents a brief description of the adiabatic compression model, which is the model of the origin of relics that is investigated in this research. Section 5 discusses of some of the properties of the galaxy cluster, Abell 3411-3412 and its relic on which this work focuses. Section 6 presents and substantiates the hypothesis of this research. And finally, section 7 gives the outline of the dissertation and the methodology.

1.1 Introduction

The Universe is understood to have evolved from the Big Bang. Observational evidence that the Universe is expanding was first found by Hubble who discovered that the radial velocity of galaxies depends on their distance (Hubble, 1929). The observed evolution of the Universe from a singularity is also in accordance with the predictions of general relativity (Hawkins & Ellis, 1965). A remarkable success of the Big Bang model was the discovery in 1965 of the cosmic microwave background (CMB) radiation (Penzias & Wilson, 1965) that was identified as the predicted left-over black-body radiation from the early stages of the Big Bang (Dicke et al., 1965). The temperature of the CMB radiation was measured with a high level of precision by the Cosmic Background Explorer to be 2.728 ± 0.004 K (Mather et al., 1990; Fixsen et al., 1996). The results from COBE, as well as the Wilkinson Microwave Anisotropy Probe (WMAP), confirm that the Universe is homogenous and isotropic, with only small anisotropies on the order of 10^{-5} (Mather et al., 1990; Hinshaw et al., 2013).

Although the cosmology of the Universe is fairly well described by the Big Bang model, there are still many open questions that are not explained within current models. These open questions include the nature of dark matter and dark energy. Evidence for dark matter was discovered around 1937 from measurements of galaxy clusters that showed that the luminous matter present in the clusters was too small for the cluster to be gravitationally bound (Zwicky, 1937; see also Trimble, 1987). Furthermore, some acceleration in the cosmic expansion has been observed and it has been postulated that this expansion is due to dark energy (Perlmutter et al., 1999).

Cosmic structures are thought to form from the small anisotropies in the density distribution of the early Universe which collapsed under gravity to form galaxies (Harrison, 1970). Galaxy clusters form in a hierarchical process as galaxies become trapped by their mutual gravitation fields (see e.g. Peebles & Yu, 1970; Press & Schechter, 1974; Kravtsov & Borgani, 2012, for a discussion of the models for the formation of clusters). The distribution of galaxy clusters in the local Universe is not homogenous but contains voids and walls (Geller & Huchra, 1989; Colless et al., 2001). These structures form what is known as the cosmic web where clusters and superclusters form at the nodes of filamentary wall-like structures.

The galaxies themselves contain millions of stars as well as interstellar gas and dust. The interstellar gas of our galaxy, for example, is made up mainly of hydrogen (70.4% by mass) with helium being the second most abundant element (28.1% by mass) and heavier elements making up only 1.5% by mass (Ferrière, 2001). Galaxies are not static as new stars are formed in the dense regions of the interstellar gas and old stars burn out and explode as either supernovae or planetary nebulae. As a result of the nuclear reactions that take place within stars, the interstellar medium becomes richer in heavy elements as the stars die out and explode (Wilson & Matteucci, 1992). The instabilities of spiral galaxies (Ostriker & Peebles, 1973), as well as their rotational curves (Bosma, 1981), indicate that galaxies contain dark matter in addition to the stars and interstellar gas and dust.

Radio astronomy is an important field within astronomy since many objects at large distances can be studied more easily in the radio wavebands than in other wavebands. Radio surveys, unlike surveys at optical frequencies, mainly detect extragalactic sources, such as active galaxies, radio quasars, and radio galaxies. Since these radio surveys can detect rare objects at large distances, they are important for investigating the isotropy of the Universe on large scales (see Ghosh et al., 2016, for a review of the role of the upcoming SKA telescope in this area). The radio band is also crucial for the detection of non-thermal emission in astronomical objects. In fact, although synchrotron emission due to relativistic electrons interacting with magnetic fields is generally not detectable in the optical waveband, it can be detected in the radio waveband. Thus, radio observations are important for studying galaxy clusters and their diffuse emission. The SKA telescope and its precursor, MeerKAT, will provide much larger and more sensitive surveys than are currently possible. The

SKA telescope is expected to be able to detect the components of a galaxy cluster up to redshifts of ~ 1. In addition, SKA1-mid will be able to provide multi-frequency data on galaxy clusters which will enable detailed studies of the spectral index of clusters which is important for understanding non-thermal cluster physics (Ferrari et al., 2015). The same authors also note that since SKA1-mid will be extremely powerful, it will be able to provide detailed studies of relatively low-luminosity radio haloes.

1.2 Galaxy clusters and their diffuse emission

Galaxy clusters are the largest gravitationally bound objects in the Universe, with typical masses of $\sim 10^{15}$ $M_{\odot}$ and typical volumes of 100 Mpc^3. Although, they can contain up to several thousands of galaxies, the cluster galaxies only make up $\sim 3-5\%$ of the total mass of a cluster with the remaining mass either in the form of dark matter ($\sim 80\%$) or dilute magnetized plasma ($\sim 15-17\%$) which forms the intracluster medium (ICM) (see e.g. Blumenthal et al., 1984; White & Fabian, 1995; Jones & Forman, 1999; Arnaud & Evrard, 1999; Sanderson et al., 2003; Vikhlinin et al., 2006, for the development of this understanding of the components of galaxy clusters). The ICM has temperatures of $10^7 - 10^8$ K and has a low particle density of $\sim 10^{-3}$ cm^{-3}. It is detected through X-ray observations as the magnetized plasma emits thermal bremsstrahlung radiation at these wavelengths (Mitchell et al., 1976; see also Sarazin, 1988 for a review of the ICM properties).

As mentioned above, galaxy clusters are formed through accretion from the filamentary structures of the Universe and through the mergers of smaller galaxy clusters or groups of galaxies. These mergers are highly energetic events that can release energies of up to $\sim 10^{64}$ ergs on time-scales of a few gigayears. This energy heats the ICM as it is dissipated through low Mach number shock waves and turbulence. Simulations suggest that accretion events produce strong shocks, while merger events produce weak shocks (Ryu et al., 2003; Pfrommer et al., 2006; Brüggen et al., 2012). Given this change in the dynamical (or merging) state of a cluster, clusters can be categorized as either relaxed (undisturbed) or merging (disturbed) (see Markevitch & Vikhlinin, 2007, for a review of cluster shock waves).

Radio observations have detected diffuse extended radio sources that are not associated with any individual galaxy but rather with the ICM itself and have no optical counterpart. Optical images of two galaxy clusters with the radio and X-ray emission overlaid are shown in Fig. 1.1. This emission is produced through synchrotron radiation as relativistic electrons (with Lorentz factors of $\gamma \gg 1000$ and particle number densities of $\sim 10^{-10}$ cm^{-3}) move in helical paths through large scale magnetic fields which have intensities of $\sim 0.1-1$ μG. The detection of these diffuse sources indicates that non-thermal components, such as large-scale magnetic fields and populations of relativistic particles, are

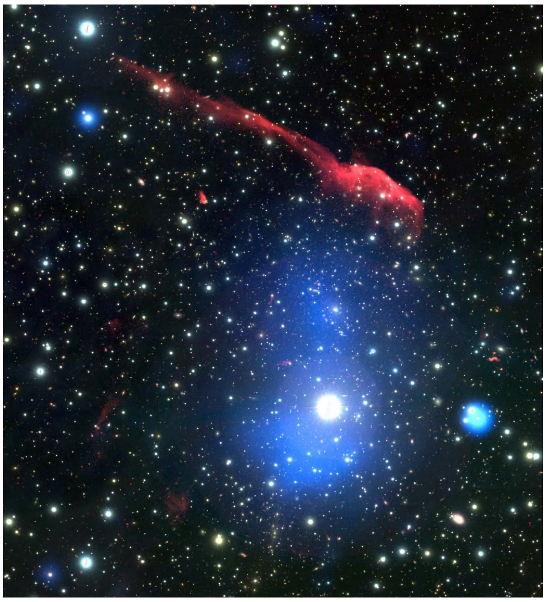

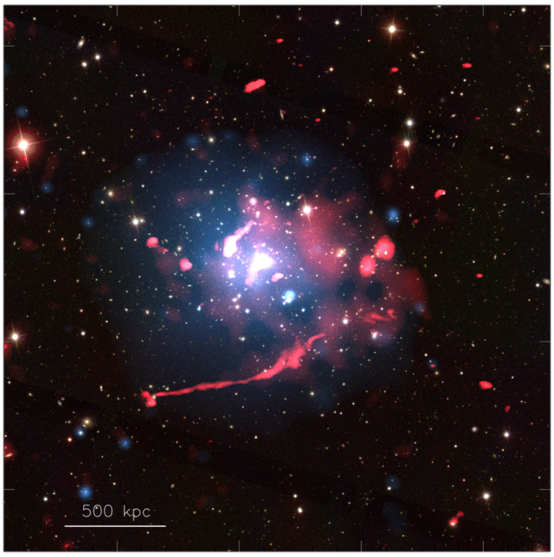

Figure 1.1: Examples of galaxy clusters. *Top panel:* Subaru *gri* colour image of the galaxy cluster 1RXS J0603.3+4214, which hosts a halo and a relic. The radio emission observed with the VLA at 1.5 GHz is shown in red and X-ray emission observed by *Chandra* in the $0.5 - 2.0$ keV band is shown in blue (Rajpurohit et al., 2018). *Bottom panel:* Optical *gri* colour image of the galaxy cluster Abell 1132, which hosts a halo and a head-tail galaxy, from the Sloan Digital Sky Survey. Radio emission observed by LOFAR is overlaid in red and X-ray emission observed by *Chandra* is overlaid in blue (Wilber et al., 2018).

mixed into the thermal plasma of the ICM (e.g. Feretti et al., 2012, for a review).

These diffuse radio sources have previously been divided into three main categories: radio haloes, radio relics, and radio mini haloes. Both radio haloes and radio relics are extended ($\gtrsim$ 1 Mpc), low-surface brightness ($\sim 1 - 0.1$ μJy arcsec^{-2} at 1.4 Ghz) sources that have a steep radio spectral index ($\alpha \leq -1, F_{\nu} \propto \nu^{\alpha}$) and that do not have optical counter parts. Radio haloes tend to occur at the centre of galaxy clusters and have a regular morphology with little to no polarization, whereas radio relics tend to occur at the cluster periphery and have either a roundish or an elongated morphology and are strongly polarized ($20 - 30\%$). Radio mini-haloes are similar to radio haloes but are less extended ($\sim$ 500 kpc) and are typically found around the brightest cluster galaxy in cool-core clusters (see e.g. Feretti et al., 2012, for a review). The most recent review of diffuse radio emission categorised the emission as radio haloes, cluster radio shocks, and revived active galactic nuclei (AGN) fossil plasma sources, phoenices and gently re-energized tails (Van Weeren et al., 2019). In this categorization scheme, sources previously categorized as mini-haloes and giant radio haloes are included in the category of radio haloes, and what was previously categorized as radio relics are called cluster radio shocks. The last category in this scheme describes sources that trace AGN radio plasma that is revived through processes in the ICM, unrelated to the galaxy. The origin of these sources and their connection to radio haloes and cluster radio shocks is still not well understood. An example of a giant radio halo and of a mini-halo is shown in Figs 1.2 and 1.3, respectively. An example of a cluster radio shock (or radio relic) is shown in Fig. 1.4.

Galaxy clusters and their diffuse emission are important objects to study in order to gain a deeper understanding of physical processes and the formation of structure in the Universe. Since galaxy clusters are virialized, they are the largest objects whose masses can be reliably measured. Thus, mass measurements of nearby clusters can be used to determine the amount of structure in the Universe on scales of $\sim 10^{14} - 10^{15}$ $M_{\odot}$ (Voit, 2005). Furthermore, studying cluster counts and the ICM mass fraction can tighten the constraints on the cosmological parameters (Allen et al., 2011). Galaxy clusters also provide unique environments to study particle acceleration physics in collisionless, high-β[1], turbulent plasmas and at weak shocks with low Mach numbers. The study of diffuse emission can also probe the large-scale structure formation of the Universe through probing the evolutionary stage of the galaxy cluster. Finally, the detection of diffuse radio emission can be used to identify shocks and turbulence in the ICM which are often difficult to identify in other wavelengths (e.g. Van Weeren et al., 2012), as well as providing a complementary method to discover clusters that were missed in X-ray, Sunyaev-Zel'dovich, or optical surveys (e.g. Macario et al., 2014; De Gasperin et al., 2017).

[1]Here β is the ratio of thermal pressure to the magnetic pressure.

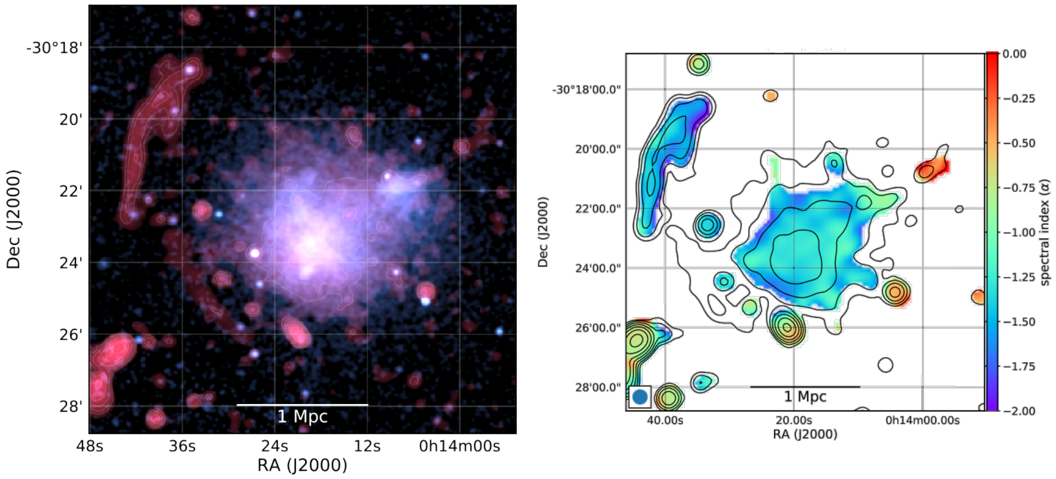

Figure 1.2: Example of a giant radio halo: giant radio halo in the cluster Abell 2744. *Left panel:* Radio emission observed with the VLA between 1 – 4 GHz is shown in red and X-ray emission observed with *Chandra* in the $0.5-2.0$ keV band is shown in blue (Pearce et al., 2017; adapted by Van Weeren et al., 2019). *Right panel:* Spectral index map between 1.5 and 3.0 GHz. The 1.5 GHz radio contours are overlaid in black at levels of $[1, 4, 16, \ldots] \times 4\sigma_{rms}$ (Pearce et al., 2017; adapted by Van Weeren et al., 2019).

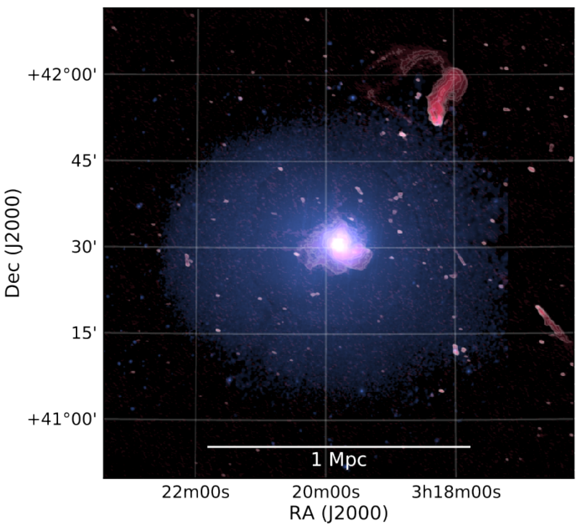

Figure 1.3: Example of a radio mini-halo: radio mini-halo hosted in the Perseus cluster. Radio emission observed by the VLA between 230 – 470 MHz is shown in red and X-ray emission observed by *XMM-Newton* in $0.4-1.3$ keV band is shown in blue (Gendron-Marsolais et al., 2017; adapted by Van Weeren et al., 2019).

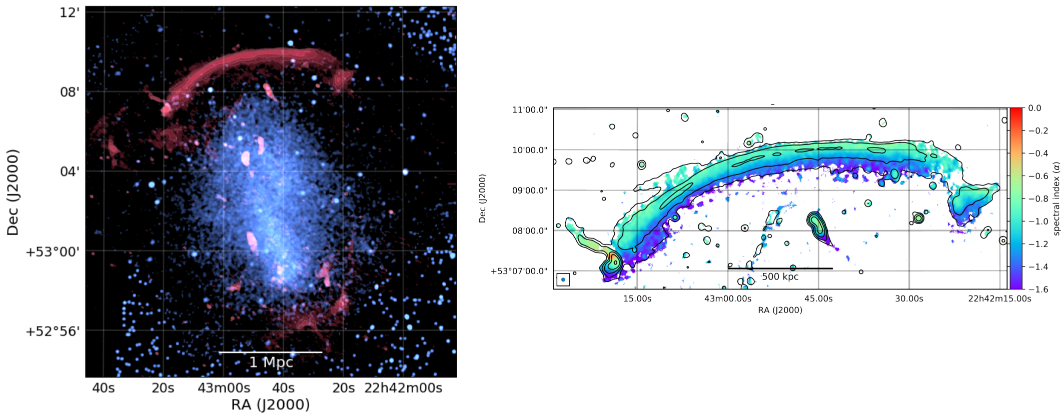

Figure 1.4: Example of a cluster radio shock (or radio relic): cluster radio shock hosted in the Sausage cluster. *Left Panel:* Radio emission observed with the GMRT at 610 MHz is shown in red (Van Weeren et al., 2010), while X-ray emission observed by *Chandra* in $0.5 - 2.0$ keV band is shown in blue (Ogrean et al., 2014). Figure is taken from Van Weeren et al. (2019). *Right Panel:* Spectral index map between 0.15 and 3.0 GHz. Radio contours from a 1–4 GHz continuum image are drawn in black at levels of $[1, 4, 16, \ldots] \times 5\sigma_{rms}$ (Di Gennaro et al., 2018; adapted by Van Weeren et al., 2019).

1.3 The problem of the origin of radio relics

The classification and understanding of the origin of relics has changed somewhat throughout the literature and has been refined in recent publications. Initially, radio relics were thought to be the remnants of radio galaxies where the galaxy had become inactive or had moved away from the relic's position (Goss et al., 1987). However, Enßlin et al. (1998) noted that, although the radio spectrum is steep, it generally does not exhibit any cut-off, as would be expected for old remnants of radio galaxies, and demonstrated that radio relics trace ICM shock fronts caused by either accretion or cluster mergers. Kempner et al. (2004) divided relics into three categories based on the acceleration mechanism producing the cosmic ray (CR) electrons: radio gischt, radio phoenices and AGN relics. Radio gischt were described as large Mpc-size sources where the electrons are accelerated at shocks by a Fermi-I acceleration process; radio phoenices were described as AGN fossil plasma that is revived through compression at a merger shock; and finally, AGN relics were described as fossil plasma that is passively evolving from a galaxy that has ceased its nuclear activity (see also Van Weeren et al., 2019). Feretti et al. (2012) did not use this classification in their review since it requires that the origin of the relic source be determined in order for it to be classified. They rather chose a classification based on the morphology of the source and classified relics as either roundish or elongated. Most recently, Van Weeren et al. (2019) used the term cluster radio shocks rather than the term radio relics and classified these as extended sources that trace particles (re-)accelerated at ICM shock waves but without requiring a particular (re-)acceleration mechanism so that it is still an observationally defined class.

A long-standing problem in the study of radio relics is the origin of the relativistic electron population. The typical diffusion length-scale in the ICM of a GeV electron within its radiative lifetime ($\lesssim 10^8$ Gyr) is of the order of 10 pc (Bagchi et al., 2002). Although plasma motions can increase this distance to some extent, it still remains less than 1 Mpc (Van Weeren et al., 2019). Thus, for Mpc-size relics, the electron cooling time is much less than the possible time since the electrons could have been injected from a galaxy at the location of the relic. This requires that an efficient particle acceleration mechanism is present within or close to radio relics (Enßlin et al., 1998; Kang et al., 2012). Enßlin et al. (1998) demonstrated that accretion or merger shock waves in the ICM could (re-)accelerate electrons within a magnetic field behind the shock front, indicating that relics trace shock waves. Further evidence of this relationship between relics and shock waves is provided by the correlation between the merger axis of the cluster and the relic position, as well as the fact that the radio power of relics scales with the X-ray luminosity and the mass of the host cluster (Vazza et al., 2015).

Although there is compelling evidence that the relativistic electron population is created through ICM shock waves, and possibly also turbulence, (re-)accelerating the electrons to relativistic energies (Van Weeren et al., 2019), there is still some debate as to the particle acceleration mechanism. A widely accepted mechanism is diffusive shock acceleration (DSA) which is based on a first order Fermi process where thermal electrons diffusing through the ICM can cross the shock front several times, each time gaining energy and eventually reaching relativistic energies (Drury, 1983; Blandford & Eichler, 1987). However, this model has several challenges. While it is fairly efficient in accelerating thermal electrons at strong shocks, at weak shocks produced by galaxy cluster mergers it is inefficient (Kang et al., 2007). Moreover, due to the higher rigidity of thermal protons compared to thermal electrons, the DSA model is more efficient at accelerating thermal protons compared to thermal electrons (e.g. Kang et al., 2007, 2012). These CR protons should then produce gamma rays as a result of collisions with thermal protons. However, the predicted theoretical value for the detection of these gamma rays is at or above the upper limit set by *Fermi* observations (e.g. Vazza & Brüggen, 2014; Vazza et al., 2015).

Another challenge to the DSA model is an observed discrepancy between the value of the shock Mach number determined within the DSA model and that determined from X-ray observations. Within the DSA model the shock Mach number is given by

$$\mathcal{M}^2 = \frac{2\alpha - 3}{2\alpha + 1}, \tag{1.1}$$

(e.g. Colafrancesco et al., 2017) where α is the radio spectral index[2] and is

[2] $F_\nu \propto \nu^\alpha$

related to the electron spectral index[3], s, by $\alpha = -(s-1)/2$. As in the case of the relic in Abell 2255 (Akamatsu et al., 2017), the shock Mach number predicted by DSA is sometimes higher than the Mach number measured from X-ray observations, indicating that the DSA model at the X-ray Mach number is not sufficient to produce the observed radio spectral index (Colafrancesco et al., 2017).

In order to explain the origin of relics better, the standard DSA model acting on the thermal electron pool was modified to a DSA model acting on a fossil population of mildly relativistic electrons (Pinzke et al., 2013). This idea is supported by observations which show that the relic is connected to a radio galaxy, which is a natural source for fossil relativistic plasma. Examples of clusters in which the relic is connected to a radio galaxy are the cluster, PLCKG287.0+32.9 (Bonafede et al., 2014), the Bullet cluster (Shimwell et al., 2015), and the cluster, Abell 3411-3412 (Van Weeren et al., 2017). While this would reduce the required efficiency of the shock, it would still not explain the lack of gamma-ray detection in galaxy clusters (Vazza & Brüggen, 2014). This would suggest that other models, not based on DSA, need to be considered as possible mechanisms for producing CR electrons in relics.

Enßlin & Gopal-Krishna (2001) proposed a model that is based on the adiabatic compression of clouds of fossil radio plasma rather than on the direct acceleration of electrons. In this model, a cloud of fossil radio plasma is accelerated as a shock wave passes around the cloud compressing it adiabatically in the process. The shock wave does not penetrate the cloud since the speed of sound within the plasma is greater than the speed of sound in the ambient medium. As the cloud of plasma is compressed, the electrons and magnetic field gain energy causing the cloud to become radio luminous. This model could explain the relative rareness of relics, since it requires both a shock wave and fossil radio plasma that has not aged too much. It could also explain the trend that relics form at the periphery of clusters, since the revive-able age of fossil plasma at the periphery is greater than that at the centre due to the stronger synchrotron losses at the centre. Furthermore, the adiabatic compression model is a more promising mechanism to revive fossil plasma due to the expected high sound speed within the radio plasma. Like DSA models, the adiabatic model can explain the thin elongated morphology of relics, since the emission is confined to a narrow shell behind the shock front (see also Zhang et al., 2019).

1.4 Brief description of the adiabatic compression model

The adiabatic compression model was described by Enßlin & Gopal-Krishna (2001) and takes place in several phases, labelled phase 0 to phase 4. The

[3] $N(\gamma) \propto \gamma^{-s}$

initial phase describes the injection of radio plasma into an expanding cocoon by an active galaxy. During phase 1 of the model, the radio cocoon continues to expand after the radio galaxy becomes inactive, causing the electrons to lose energy adiabatically. In addition, the magnetic field is weakened by the expansion. This, and the adiabatic energy losses of the electrons, can result in the radio emission of the cocoon becoming undetectable. In the second phase of the model, the radio plasma is in pressure equilibrium with the environment and the electrons exist at low energies as a result of the previous adiabatic losses. Since the radiative losses depend on the particle energy, these losses are suppressed during this phase. This fossil plasma is revived during the phase three, where the plasma is compressed during a shock passage caused by a merger event. This compression causes the electron population and the magnetic field to gain energy adiabatically leading to a sharp increase in the synchrotron emissivity. During the final, fourth phase of the model, the plasma is again in pressure equilibrium with the post-shock medium and the synchrotron emission of the relic fades away as a result of the heavy radiative losses.

Enßlin & Gopal-Krishna (2001) studied three different scenarios of the model. The first scenario investigated the radio emission of revived plasma located at the cluster centre. They found that the compression caused a burst of low frequency emission but almost no high frequency emission and the source was found to decay on a time-scale of a few tens of megayears. They noted that in the peripheral regions of the cluster the density, pressure and magnetic field are lower which would decrease the radiative losses and lengthen the time-scale over which the fossil plasma can still be revived by a shock wave. The second scenario that they investigated examined the emission of a radio cocoon at the cluster boundary that was born outside of the cluster. They found that this scenario could explain the steep and bent radio spectrum of the relic hosted in Abell 85. The third scenario was similar to the second, but they chose a shorter duration of phase 2 which resulted in a relatively flat, unbent spectrum. They concluded that the model provides a promising and natural explanation of radio relics.

1.5 The galaxy cluster Abell 3411-3412 and its radio relic

The galaxy cluster Abell 3411-3412 (hereafter A3411-3412) hosts an irregularly shaped radio relic $\sim$ 1.9 Mpc long that is made up of several regions or sub-relics (Van Weeren et al., 2013). The cluster is undergoing a merging event where the projected merger axis lies along the SE-NW direction (Van Weeren et al., 2013). The two merging galaxy sub-clusters have similar masses ($\sim 10^{15}$ $M_\odot$) and the cluster is viewed $\sim$ 1 Gyr after the core passage (Van Weeren et al., 2017). The compact core of the sub-cluster that came from the south has survived the collision up to now, while the gas core of the sub-cluster that came from the north was largely disrupted during the core passage. X-ray observations of the south-eastern region of the cluster have shown that a shock with a Mach number between 1.2 – 1.7 is coincident with the position of the relic (Van Weeren et al., 2017).

Van Weeren et al. (2017) studied this galaxy cluster and the relic in the optical, radio and X-ray wavebands. Their observations of the north-eastern component or sub-relic show that this component is $\sim$ 150 kpc long and is connected through a radio tail to one of the cluster galaxies located $\sim$ 90 kpc to the north. An image of this cluster and its relic is given in Fig. 4.1. The presence of the radio tail indicates that this galaxy could have provided seed electrons that have been revived. The same authors also measured the spectral properties of the relic and found that the spectral index steepens with distance away from the galaxy nucleus, which is consistent with synchrotron and inverse Compton losses. Where the relic joins the radio tail the spectral index flattens somewhat, while along the length of the relic the spectral index is fairly uniform. More detail about the galaxy cluster and the relic it hosts is presented in chapter 4.

Van Weeren et al. (2017) applied a DSA-type re-acceleration model to this north-eastern component of the relic. The modelling they performed can explain the uniform spectral index along this relic. However, it could have difficulties explaining the constant spectral indices along the lengths of Mpc-size relics, unless the shock has a high Mach number or the spectral index distribution of the fossil plasma is fairly uniform. Their modelling also predicted a value of 1.9 for the shock Mach number which is greater than the limit of the observed X-ray Mach number.

1.6 Hypothesis

This project investigates whether the adiabatic compression model is a plausible model for the formation of the radio relic hosted in the galaxy cluster A3411-3412 by investigating whether the adiabatic compression model is able to reproduce the observed spectral shape across the relic. The fossil electron cloud required in the adiabatic model is provided, as in the DSA case studied by Van Weeren et al. (2017), by the radio galaxy that is connected to the relic through a narrow radio tail. Although Van Weeren et al. (2017) were able to reproduce the spectral properties of the relic using a DSA-type re-acceleration model, their modelling predicted a higher Mach number compared to the Mach number determined through the X-ray observations. This project will investigate whether the adiabatic model can reproduce the radio flux density and spectral shape of the relic with a lower Mach number. Furthermore, in light of the recent observational and theoretical challenges to DSA based models, there is a need to investigate other models for the origin of radio relics.

Other objectives of the project are: to extend the adiabatic compression scenario to the case of an electron population that has a general initial energy spectrum; to understand how this scenario works in the specific case of a shock with a low Mach number as in the case of A3411-3412; and, to understand if the evolution of the electron spectrum after the compression is determined only by radiative energy losses, or if there are other effects, such as post-shock turbulence or an expansion phase following the compression phase, that impact the spectrum evolution. Finally, this project also investigates whether sources that are classified as radio gischt can be explained by adiabatic compression and not just radio phoenices, suggesting that revived fossil plasma could be the origin of both sources.

1.7 Outline and methodology

The dissertation is structured as follows.

Chapter 2 will present a brief overview of the formalism of synchrotron radiation. The expected radio synchrotron emission at the end of the radio tail is also calculated using this formalism and the results are discussed in light of the observational results published in Van Weeren et al. (2017). In particular, this chapter will investigate whether the electron spectrum given as

$$N(\gamma) = \tilde{N}_0 \gamma^{-2.5} \exp\left(-(\gamma/\gamma_c)^2\right), \tag{1.2}$$

where γ is the Lorentz factor and $\gamma_c = 1.8 \times 10^4$ is the Lorentz cut-off factor, can explain the observations of the radio tail injected by the galaxy before the compression by the shock and calculate the value of the normalization constant, $\tilde{N}_0$.

Chapter 3 will present the formalism of the the adiabatic compression model and expand the model to act on a generalized electron spectrum given as a power-law with an exponential cut-off:

$$N(p) = \tilde{N}_0 p^{-s} \exp\left(-\left(p/p_c\right)\right), \tag{1.3}$$

where p is the dimensionless momentum of a single electron and p_c is the cut-off momentum. For ultra-relativistic electrons considered here, the dimensionless single-electron momentum is equivalent to the Lorentz factor. The formalism presented in this section follows the steps outlined in Enßlin & Gopal-Krishna (2001). Finally, this chapter will also investigate the effect that the shock strength of the associated cluster shock wave has on the resulting radio spectrum, as well as the effect that some of the model parameters have on the radio spectrum.

Chapter 4 will apply the adiabatic model to the radio relic hosted in the galaxy cluster A3411-3412. Starting with an electron spectrum that describes the electron population that is injected by the galaxy, the evolution of this spectrum through the phases of the adiabatic model will be calculated using the results of chapter 3. From these electron spectra the expected radio spectra at the end of each phase of the model will be calculated using the standard synchrotron formulae presented in chapter 2. The spectral indices of these spectra will be compared to the observed spectral indices at corresponding points across the relic. Finally, the radio spectrum behind the shock front will be investigated to see if the evolution behind the shock front is only determined by radiative losses, or if other mechanisms such as an expansion phase or post-shock turbulence affect the spectrum.

Lastly, chapter 5 will summarize the results of each chapter and discuss the ability of the adiabatic compression model to reproduce the spatial distribution of the relic in A3411-3412 and its ability to describe the relic's formation.

The equations describing the electron and radio spectra were implemented in Python functions and these were used to calculate the luminosities and flux densities presented in this work. The properties of the galaxy cluster that were used in the modelling performed in this work were taken from Van Weeren et al. (2017) and the results that were found were compared to the observational results published by the same authors.

Chapter 2

Synchrotron emission of the radio tail and the initial electron spectrum

2.1 Introduction

Van Weeren et al. (2017) report that in the cluster of interest, Abell 3411-3412, a cluster galaxy is located $\sim$ 90 kpc to the north of the radio relic. This cluster galaxy has an active galactic nucleus (AGN) at its centre and a radio tail connects the galaxy to the relic. The steepening of the radio tail's spectral index from a value of $\alpha = -0.5$ at the galaxy nucleus to a value of $\alpha = -1.3 \pm 0.1$ at the further end of the tail is consistent with synchrotron and inverse Compton losses. At the position where the radio tail meets the relic, the spectral index flattens to $\alpha = -0.9$ which, according to the same authors, indicates that the electron population of the radio tail is re-accelerated at the position of the shock. Thus, the radio tail could provide a fossil population of electrons that can be revived to form the radio relic.

Since the radio emission of relics is produced through synchrotron radiation of electrons, we will here provide a brief formalism of synchrotron radiation. This formalism will then be applied to the electron spectrum of the radio tail as given by Van Weeren et al. (2017) and the resulting spectral index will be compared to the observed one in order to confirm that this electron spectrum can explain the properties of the radio tail before the action of the shock wave. Furthermore, we will also calculate the normalization constant of the electron spectrum in order to completely describe the electron population of the radio tail that will be used in chapter 4.

2.2 Formalism of synchrotron radiation

As electrons move in helical paths through a magnetic field, they emit synchrotron radiation. The total power, L_ν, radiated by an isotropic population of electrons, that has a number density $N(\gamma)\mathrm{d}E$, is the integral over all energies of the product of the power radiated by a single electron, $P_{\rm sync}$, and the electron energy number density (or electron spectrum):

$$L_\nu = \int_{\gamma_{min}}^{\gamma_{max}} \mathrm{d}\gamma \, N(\gamma) P_{\rm sync}(\nu, \gamma), \tag{2.1}$$

where γ is the Lorentz factor. The synchrotron power of a single relativistic electron is given by

$$P_{\rm sync}(\nu, \theta, \gamma) = 2\pi\sqrt{3}\, r_0 m c \nu_0 \sin(\theta)\, F(x/\sin\theta) \tag{2.2}$$

(Schlickeiser, 2002), where

$$x = \frac{2\nu}{3\nu_0\gamma^2}\left[1 + \left(\frac{\gamma\nu_p}{\nu}\right)^2\right]^{3/2}, \tag{2.3}$$

and $r_0 = e^2/\left(mc^2\right)$ is the classical electron radius, $\nu_0 = eB/\left(2\pi mc\right)$ is the non-relativistic gyrofrequency and $\nu_p = 8980 n_e$ is the plasma frequency. Here n_e is the thermal electron density, for which a typical value is 10^{-4} cm^{-3}. The spectral function, $F(t)$, is given by

$$F(t) \equiv t \int_t^\infty \mathrm{d}z\, K_{5/3}(z), \tag{2.4}$$

where $K_{5/3}(z)$ is the modified Bessel function of the second kind.

Integrating eqn (2.2) over the solid angle, $\mathrm{d}\Omega = \sin\theta\,\mathrm{d}\phi\,\mathrm{d}\theta$, gives

$$P_{\rm sync}(\nu, \gamma) = 2\pi\sqrt{3} r_0 m c \nu_0 \int_0^\pi \mathrm{d}\theta\, \frac{1}{2}\sin^2\theta\, F\left(\frac{x}{\sin\theta}\right), \tag{2.5}$$

where the integral over the azimuthal angle, ϕ, has been performed. This expression for the synchrotron power of a single electron can then be substituted into eqn (2.1) to calculate the emitted synchrotron power, or luminosity, of an electron population.

In order to save on computational time, the following approximation for the spectral function was used in the implementation of these formulae (Schlickeiser, 2002):

$$F(t) \simeq 1.78\, t^{0.3} e^{(-t)}. \tag{2.6}$$

The flux density of the electron population can then be calculated from the luminosity according to

$$F_\nu = \frac{1}{4\pi D_L^2} L_\nu, \tag{2.7}$$

where L_ν is the total synchrotron power of the electron population as given in eqn (2.1) and D_L is the luminosity distance.

For a power-law electron distribution, $N(\gamma) \propto \gamma^{-s}$, where s is the electron spectral index, it can be shown that the synchrotron luminosity also follows a power-law:

$$L_\nu \propto \nu^\alpha, \tag{2.8}$$

where $\alpha = -(s-1)/2$ is the radio spectral index (Rybicki & Lightman, 1979). For general electron population the spectral index is defined in terms of the flux density to be $F_\nu \propto \nu^\alpha$ and can be calculated between any two frequencies at which the flux density is known.

2.3 Synchrotron spectral index between 0.325 and 3.0 GHz

The initial electron spectrum of the radio tail is given by Van Weeren et al. (2017) to be

$$N(\gamma) = \tilde{N_0}\gamma^{-2.5} \exp\left(-(\gamma/\gamma_c)^2\right), \tag{2.9}$$

where the normalization constant $\tilde{N_0}$ has to be determined (see section 2.4) and γ_c is the cut-off Lorentz factor. Van Weeren et al. (2017) chose the value of $\gamma_c = 1.8 \times 10^4$ to match the radio spectral index of $\alpha = -1.3$ between 0.325 and 3.0 GHz. This electron spectrum is shown by the solid blue line in Fig. 2.1. As expected, this figure shows that the number density follows a power-law relationship for $\gamma \leq \gamma_c$ while for $\gamma > \gamma_c$ it drops off exponentially.

The synchrotron luminosity of this electron population was calculated according to eqn (2.1) using the value of the pre-shock magnetic field, $B = 1.5\ \mu$G as given in Van Weeren et al. (2017). The resulting radio spectrum is shown by the solid blue line in Fig. 2.2. The slope of the spectrum at low frequencies, as shown by Fig. 2.2, is $\alpha = -0.75$ as would be expected for an initial power-law distribution of electrons with a slope of $s = 2.5$. This slope changes around 1 GHz where the exponential cut-off in the electron distribution starts to take effect, and above 10 GHz the power drops off quickly.

In order to ensure that the Python routines that were written to calculate the luminosity are reliable, the radio spectral index between 325 MHz and 3.0 GHz of this population was calculated and found to be $\alpha = -1.3$. This matches the observed value of the spectral index at the end of the radio tail (see the radio spectral index map Fig. 3b in Van Weeren et al. (2017)) which confirms that the routines are reliable and can be used in the subsequent work.

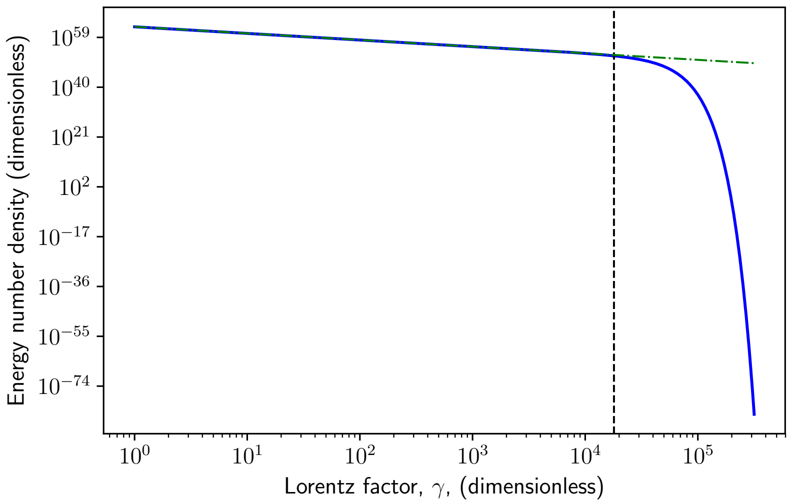

Figure 2.1: The calculated electron spectrum at the end of the radio tail where the electron population follows a power-law with an exponential cut-off (see eqn (2.9)) is shown in the solid blue line and is compared to the calculated electron spectrum of a population that follows a pure power-law, shown in the dot-dashed green line. At the cut-off Lorentz factor, indicated by the dashed black vertical line, the electron spectrum at the end of the radio tail starts to drop rapidly below the power-law spectrum, showing that the exponential term dominates from this point on.

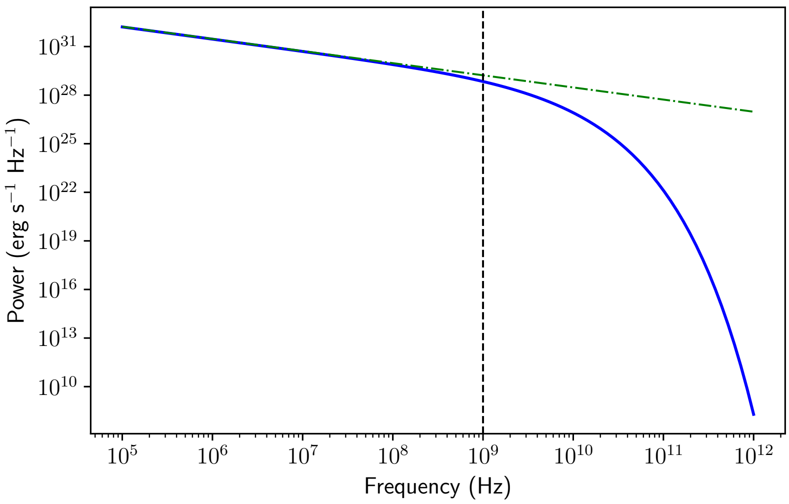

Figure 2.2: The calculated synchrotron luminosity of the electron population in the radio tail before the shock wave is shown in the solid blue line. Again, the comparison to the calculated luminosity of a pure power-law electron population (shown in the dot-dashed green line) shows that the luminosity of the radio tail starts to fall below the luminosity of the power-law population around 1 GHz (indicated by the dashed black vertical line) indicating that the exponential factor in the electron distribution starts to dominate from this point on.

2.4 Normalization of the electron population

The second purpose of calculating the synchrotron emission in the radio tail was to calculate the value of the electron normalization, $\tilde{N}_0$, so that the electron population of the radio tail is fully determined. The normalization constant was determined by matching the calculated flux density to the observed flux density of the radio tail presented in Van Weeren et al. (2017).

The flux density of the electron population was calculated from the spectral luminosity according to eqn (2.7). In order to apply this equation, the luminosity distance was calculated using an online cosmological calculator (Wright, 2006) with the following values of the cosmological parameters: $\Omega_M = 0.27$, $\Omega_\lambda = 0.73$ and $H_0 = 71$ km s^{-1} kpc^{-1} (Van Weeren et al., 2013) and a redshift of 0.164 which corresponds to the redshift of the galaxy connected to the radio tail (Van Weeren et al., 2017). The calculated angular scale conversion factor was 167.1 kpc arcmin^{-1} which is sufficiently close to the angular conversion factor of 168 kpc arcmin^{-1} used in Van Weeren et al. (2017) (see Fig. 8 therein). The luminosity distance obtained in this way was $D_L = 778.3$ Mpc and this was used to calculate the flux density from the calculated synchrotron luminosity.

Van Weeren et al. (2017) extracted observed flux densities at intervals of 20 kpc across the relic and somewhat to the south of the radio tail. These flux densities are presented in Fig. 4.5. Comparing the values of the spectral index plotted in this figure to the spectral index map published in Fig. 3b of the same paper, indicates that the distances given in the figure are measured from some point on the outer edge of the relic. The flux density of the radio tail should be unaffected by the compression caused by the shock wave. Thus, the flux density of the radio tail was taken to be given by the flux density at 610 MHz at 200 kpc which is 176 μJy.

The calculated flux density was matched to this observed flux density by varying the value of the normalization constant, $\tilde{N}_0$. The best-fitting value of the normalization constant obtained in this way was $\tilde{N}_0 = 1.1 \times 10^{63}$. The calculated flux density using this value is shown in Fig. 2.3.

The flux density shown in Fig. 2.3 shows the same features as the spectral luminosity, namely, that the spectral index has a value $\alpha = -0.75$ at low frequencies, as expected for a power-law electron population with a slope of 2.5, and begins to steepen around 1 GHz.

2.5 Conclusion

This chapter presented the formalism of synchrotron radiation. Since the radio emission of relics is due to synchrotron radiation, this formalism is used throughout the rest of this work.

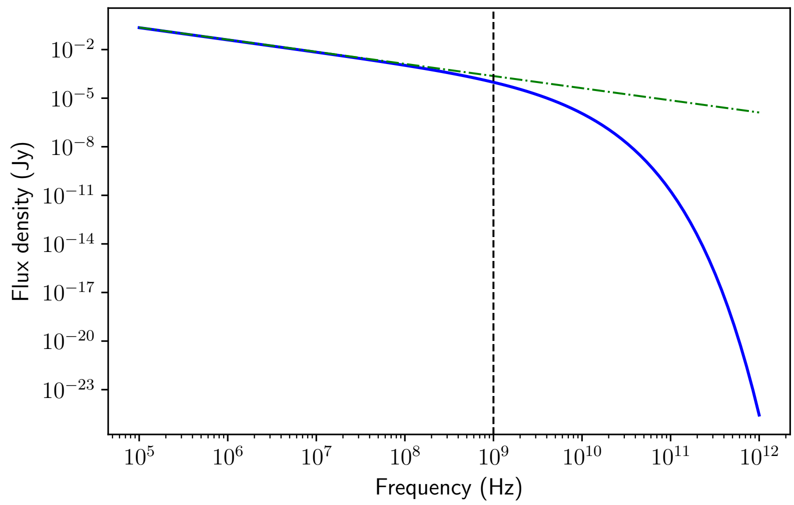

Figure 2.3: The calculated flux density of the electron population in the radio tail before the compression caused by the shock wave is shown in the solid blue line. As in Fig. 2.2, the flux density starts to fall below the flux density of a power-law electron population (shown in the dot-dashed green line) around 1 GHz (indicated by the dashed black vertical line).

This chapter also shows the calculation of the spectral index of the resulting luminosity where the initial electron spectrum is given by eqn (2.9). This spectral index matches the observed spectral index at the end of the radio tail indicating that synchrotron radiation with this initial spectrum can explain the observations of the radio tail before the compression of the shock wave.

Finally, the normalization of the electron population was also calculated. The value of this normalization constant is important since the electron population of the radio tail will be used in further calculations in chapter 4 and so needs to be fully described. Since the value of the flux density at the position of the radio tail is not available, the flux density was assumed to be given by the value of the flux density just before the inner edge of the relic. However, the flux density at this position was only available at one frequency. In future studies, to obtain more refined results, it would be necessary either to obtain the data used by Van Weeren et al. (2017) or to use new observations of this cluster from telescopes such as the MeerKAT.

Chapter 3

The adiabatic compression model

3.1 Introduction

In this chapter, the adiabatic model developed by Enßlin & Gopal-Krishna (2001) is investigated. Firstly, the model is extended to a more general electron population that follows a power-law with an exponential cut-off at large Lorentz factors. Secondly, the effects of different shock strengths and different time-scales of the shock passage on the shape of the radio spectrum are investigated.

The adiabatic compression model describes several phases in which radio plasma undergoes expansion and compression. The radio plasma is injected into a cocoon by a nearby radio galaxy, loses energy as the cocoon expands, is re-energized as a result of the compression caused by the passage of a cluster shock wave, and finally fades away due to radiation losses. The electron spectrum and, consequently, the resulting radio spectrum are shaped by the compression or expansion of the radio cocoon as well any radiative energy losses during each phase. Unlike in the DSA model or in the DSA-type re-acceleration model, in the adiabatic model the shock wave does not penetrate the cloud of fossil plasma due to the high sound speed within the plasma compared to the sound speed in the thermal surrounding. Instead, the fossil plasma is compressed as the shock wave passes through the surrounding thermal plasma. This adiabatic compression causes the fossil electrons to gain energy adiabatically while also amplifying the magnetic field, leading to a steep enhancement of the radio emission of the radio plasma cocoon.

Following the convention used by Enßlin & Gopal-Krishna (2001), the phases of the model are labelled phase 0 to phase 4. Phase 0 is the injection phase of the model, where a nearby active galaxy injects radio plasma into an expanding volume. This phase is not a complete phase in the model as it describes the conditions within the plasma at the end of the galaxy's activity but it does not describe the complete injection process.

Phase 1 describes the expansion of the radio cocoon after the activity of the radio galaxy has ceased. During this phase, the radio cocoon is strongly over-pressured compared to the surrounding thermal gas, which causes the cocoon to expand until pressure equilibrium with the environment is reached. As a result of this expansion, the electrons lose energy adiabatically and the magnetic field strength is reduced, leading to a decrease in the radio emission. The radio plasma can be described as fossil radio plasma as the radio emission is probably much fainter than the emission at the end of phases 0, 3 and 4. For example, in scenarios B and C presented in Enßlin & Gopal-Krishna (2001), the radio luminosity drops by a factor of between 1 and 3 orders of magnitude at low frequencies (0.1 – 0.5 GHz) and 4 or more at high frequencies (1 – 10 GHz), showing that the radio emission at the end of this phase can be very faint and can have a very steep spectrum, making it difficult to detect. These adiabatic losses due to the expansion of the cocoon are, however, reversible and will be reversed during phase 3.

Phase 2 is a dormant phase where the volume of the radio plasma remains largely unchanged. Due to the adiabatic losses of the previous phase, the electron energy and the magnetic field energy density are greatly reduced. Since radiation losses depend on the particle energy as well as the magnetic field energy, the radiative losses during this phase are very low. The suppression of the irreversible radiative losses during this phase enables the cocoon to maintain its energy (Enßlin & Gopal-Krishna, 2001) so that the radio plasma can be revived in the next phase when the adiabatic losses are reversed.

Phase 3 is the main phase in the model. During this phase the cocoon of fossil plasma is compressed by the passage of a shock wave in the surrounding thermal medium. The shock wave is caused by a merger or accretion event in the galaxy cluster. For a given shock speed, v, the Mach number ($\mathcal{M} = v/c_s$, where c_s is the sound speed in the medium) will be much smaller for a higher sound speed. Therefore, because of the higher speed of sound within the radio cocoon as compared to the surrounding thermal gas, the same shock will have a much smaller Mach number within the cocoon than within the surrounding gas. Thus, the shock wave is not expected to penetrate the radio cocoon or to accelerate the electrons via DSA, but instead the shock wave is expected to compress the cocoon (Enßlin & Gopal-Krishna, 2001; Colafrancesco et al., 2017). This adiabatic compression reverses the adiabatic losses of phase 1 and the electrons within the plasma, as well as the magnetic field, gain energy adiabatically, leading to a steep increase in the synchrotron emissivity. Since the electrons are re-energised by the compression of the radio cocoon, this phase has the flattest radio spectrum. During this phase, the cocoon expands orthogonally to the direction in which the shock is moving while being compressed in the direction of the shock, forming the typical flattened, arc-like shape of radio relics.

Phase 4 is the final phase in the model. As in phase 2, the radio plasma is in pressure equilibrium with its surroundings so the plasma volume remains more or less constant throughout the phase. As a result of the energy gains in the previous phase, the radio plasma now suffers heavy radiation losses resulting in a steep radio spectrum and causing the radio emission of the relic to fade away.

3.2 Formalism

3.2.1 Changes in the electron momentum due to adiabatic and radiative losses or gains

As described above, the electron spectrum and the resulting radio spectrum are shaped by the energy gains or losses as well as any volume changes during each phase. This section outlines the formalism of such changes to the electron spectrum. Following the steps outlined by Enßlin & Gopal-Krishna (2001), the adiabatic model is extended to an electron population that is described by a power-law with an exponential cut-off at large values of the Lorentz factor (or, equivalently the dimensionless momentum, p). An expression for the resulting electron spectrum of such a population is then derived.

Changes in the dimensionless momentum, $p = P_{\mathrm{e}}/(mc)$, of an ultra-relativistic electron depend on: the synchrotron losses, which are proportional to the magnetic energy density, u_{B}; the inverse Compton losses, which are proportional to the cosmic microwave background (CMB) radiation field energy density, u_{C}; and the adiabatic losses or gains connected to the change in volume, V, of the radio plasma. The electrons in the cocoon either lose or gain energy adiabatically as the volume expands or contracts, since the electron gas is either doing work on the environment, or the environment is doing work on the electron gas. The change in the internal energy, U, when the volume changes from V to $V + \mathrm{d}V$ is

$$\mathrm{d}U = -P\mathrm{d}V, \tag{3.1}$$

where P is the pressure of the electron gas. Then, working in terms of the momentum rather than energy, the change in the electron momentum as a result of adiabatic gains or losses can be shown to be

$$-\frac{\mathrm{d}p}{\mathrm{d}t} = \frac{1}{3}\frac{1}{V}\frac{\mathrm{d}V}{\mathrm{d}t}p \tag{3.2}$$

(Longair, 2011). Together with the synchrotron and inverse Compton losses, the change in the dimensionless momentum is given by the following differential equation:

$$-\frac{\mathrm{d}p}{\mathrm{d}t} = a_0\left(u_{\mathrm{B}} + u_{\mathrm{C}}\right)p^2 + \frac{1}{3}\frac{1}{V}\frac{\mathrm{d}V}{\mathrm{d}t}p, \tag{3.3}$$

where $a_0 = \frac{4}{3}\sigma_{\mathrm{T}}/(mc)$ and σ_{T} is the Thomson cross section. Due to the low particle density within the radio plasma, the model does not include the effects of bremsstrahlung and Coulomb losses (Enßlin & Gopal-Krishna, 2001). Furthermore, the model assumes that there is sufficient pitch angle scattering so that the electron pitch angle remains isotropic. This is a realistic assumption since the cosmic ray (CR) electrons will scatter off the thermal plasma due to wave particle interactions which will result in pitch angle scattering (Jaffe & Perola, 1973).

Introducing the compression ratio, defined as

$$C(t) = \frac{V_0}{V(t)}, \tag{3.4}$$

where V_0 is the volume of the radio plasma at some initial time, t_0, and using the change of variable $\tilde{p}(t) = C(t)^{-1/3}p(t)$, eqn (3.3) can be transformed into the following differential equation:

$$\frac{\mathrm{d}\tilde{p}}{\mathrm{d}t} = -a_0\,(u_{\mathrm{B}} + u_{\mathrm{C}})\,C(t)^{1/3}\tilde{p}(t)^2. \tag{3.5}$$

This equation can then be solved by integrating to give

$$\tilde{p}(t)^{-1} - \tilde{p}_0^{-1} = a_0 \int_{t_0}^{t} \mathrm{d}t'\,(u_{\mathrm{B}}(t') + u_{\mathrm{C}}(t'))\,C(t')^{1/3}, \tag{3.6}$$

where $\tilde{p}_0 = \tilde{p}(t_0) = C(t_0)^{-1/3}p(t) = p_0$ since $C(t_0) = 1$ and where p_0 is the electron momentum at the initial time t_0. By defining the characteristic momentum to be

$$\frac{1}{p_*(t)} = a_0 \int_{t_0}^{t} \mathrm{d}t'\,(u_{\mathrm{B}}(t') + u_{\mathrm{C}}(t'))\left(\frac{C(t')}{C(t)}\right)^{\frac{1}{3}}, \tag{3.7}$$

eqn (3.5) can be simplified to

$$\tilde{p}(t)^{-1} = \frac{C(t)^{1/3}}{p_*(t)} + \tilde{p}_0^{-1}. \tag{3.8}$$

Finally, changing variables back to the dimensionless momentum, p, gives

$$p(p_0, t) = \frac{p_0}{C(t)^{-\frac{1}{3}} + p_0/p_*(t)}. \tag{3.9}$$

In order to evaluate the integral in eqn (3.7), it is assumed that the volume changes according to a power-law in time, i.e.,

$$V(t) = V_0\left(\frac{t}{t_0}\right)^{b}, \text{ or } C(t) = \left(\frac{t}{t_0}\right)^{-b}, \tag{3.10}$$

that the photon energy density is constant and that the magnetic field energy density scales as

$$u_{\rm B}(t) = u_{\rm B,0}\left(\frac{V}{V_0}\right)^{-\gamma_{\rm B}} = u_{\rm B,0}\left(\frac{t}{t_0}\right)^{-\gamma_{\rm B}b} = u_{\rm B,0}\left(\frac{t}{t_0}\right)^{-4b/3}, \tag{3.11}$$

where $\gamma_{\rm B} = 4/3$ is the adiabatic index of the magnetized plasma (Kaiser et al., 1997). Then, evaluating the integral gives

$$p_*(t) = \frac{C^{1/3}}{a_0 t\left(\frac{C^{5/3}-C^{1/b}}{1-5b/3}u_{\rm B\,0} + \frac{C^{1/3}-C^{1/b}}{1-b/3}u_{\rm C}\right)}, \tag{3.12}$$

where, to simplify the notation, $C = C(t)$. Note that it is reasonable to assume that the photon energy is constant since it is dominated by the CMB which does not change significantly over the time-scales under consideration (Enßlin & Gopal-Krishna, 2001). The cases $b = 3/5$ and $b = 3$ are excluded for simplicity as they produce logarithms rather than power-laws.

In summary, the momentum of an ultra-relativistic electron within the radio plasma depends on the synchrotron losses, the inverse Compton losses and the adiabatic gains or losses that result from the change in volume of the radio plasma. Then, under the assumptions of eqns (3.10) and (3.11), the momentum at time t of an electron which has an initial momentum p_0 at an initial time t_0 is given by eqn (3.9) together with eqn (3.12).

3.2.2 The electron spectrum of a single adiabatic cooling phase

The electron spectrum is shaped by the radiative and adiabatic losses or gains described in the previous section. At any given time, the electron distribution per volume and momentum, $N(p,t)\mathrm{d}p\,\mathrm{d}V$, for $p < p_*(t)$ is

$$N(p,t) = N_0\left(p_0(p,t)\right)\frac{\partial p_0(p,t)}{\partial p}C(t), \tag{3.13}$$

where the initial momentum $p_0(p,t)$ is obtained from eqn (3.9):

$$p_0(p,t) = \frac{p\,C(t)^{-1/3}}{1-p/p_*(t)}. \tag{3.14}$$

For any initial distribution, $N_0(p_0)$, the resulting electron distribution, $N(p,t)$, at $p = p_*(t)$ exhibits a sharp upper cut-off due to synchrotron and inverse Compton losses. Thus, the characteristic momentum, $p_*(t)$, is also the maximal momentum.

Since this project extends the adiabatic model to act on a more general electron spectrum, the initial distribution is chosen to follow a power-law with an exponential cut-off for p greater than some cut-off value p_c:

$$N_0(p_0) = \tilde{N}_0\,p_0^{-s}\exp\left(-(p_0/p_c)^2\right), \tag{3.15}$$

for $p_{\min 0} < p_0 < p_{\max 0}$. This distribution function is an extension of the electron spectrum of the radio tail connected to the relic in the galaxy cluster A3411-3412 (Van Weeren et al., 2017), where the distribution is given in terms of the dimensionless electron momentum, p, rather than in terms of the Lorentz factor, γ, since these two quantities are basically equivalent for ultra-relativistic electrons.

The resulting electron distribution is determined according to eqn (3.13). From eqn (3.14), we have

$$\frac{\partial p_0(p,t)}{\partial p} = C(t)^{-1/3}\left(1 - \frac{p}{p_*(t)}\right)^{-2}, \tag{3.16}$$

and,

$$N_0\left(p_0(p,t)\right) = \tilde{N}_0\, C(t)^{s/3}\left(1 - \frac{p}{p_*(t)}\right)^{s} p^{-s} \exp\left(-\left(\frac{p\, C(t)^{-\frac{1}{3}}}{p_c\,(1 - p/p_*(t))}\right)^{2}\right). \tag{3.17}$$

Substituting eqns (3.16) and (3.17) into eqn (3.13) gives the resulting electron spectrum for $p_{\min}(t) = p(p_{\min 0}, t) < p < p_{\max}(t) = p(p_{\max 0}, t)$:

$$N(p,t) = \tilde{N}_0\, C(t)^{\frac{s+2}{3}} p^{-s}\left(1 - \frac{p}{p_*(t)}\right)^{s-2} \exp\left(-\left(\frac{p\, C(t)^{-\frac{1}{3}}}{p_c\,(1 - p/p_*(t))}\right)^{2}\right). \tag{3.18}$$

Physically, this equation describes how the electron distribution has been shaped by the energy losses or gains described by eqn (3.3).

3.2.3 Resulting electron and radio spectrum after several adiabatic cooling phases

As discussed in section 3.1, the adiabatic compression scenario involves several phases of expansion or compression that are characterised by different rates and durations. Each of these phases contribute to the final shape of the electron distribution making it necessary to describe the momentum and the electron spectrum at the end of n expansion or compression phases. The following notation is used to label the parameters of each phase: $p_1 = p(t_1)$ is the momentum of an electron at the end of phase 1 where its original momentum is p_0; the compression ratio characterizing this phase is $C_{0\,1} = C(t_1)$ and the characteristic momentum at the end of the phase is $p_{*0\,1} = p_*(t_1)$. Similarly, p_2 is the momentum of the same electron after phase 2 which is characterised by the compression ratio $C_{1\,2}$ and the characteristic momentum $p_{*1\,2}$. And so on, for the other phases.

From eqn (3.9), it follows that the final momentum, p_n, after n such phases is

$$p_n(p_0) = \frac{p_0}{C_{0\,n}^{-1/3} + p_0/p_{*\,0\,n}}, \tag{3.19}$$

where $C_{0\,n}$ is the compression ratio between the initial and final configurations:

$$C_{0\,n} = \prod_{i=1}^{n} C_{i-1\,i} = \prod_{i=1}^{n} \frac{V_{i-1}}{V_i} = \frac{V_0}{V_n}. \tag{3.20}$$

The characteristic momentum between the n'th phase and the initial configuration is the sum of the individual cooling phases, each weighted by $(C_{0\,i})^{1/3}$:

$$\frac{1}{p_{*0\,n}} = \sum_{i=1}^{n} \frac{(C_{0\,i-1})^{1/3}}{p_{*\,i-1\,i}}. \tag{3.21}$$

Note that, from eqn (3.10), $C_{0\,0}$ is by definition equal to unity: $C_{0\,0} = (t_0/t_0)^{-b} = 1$. This is necessary for the above equation to make sense with $n = 1$.

Each phase is fully described by a set of four parameters: the expansion or compression exponent, b_i (see eqn (3.10)), the time-scale of expansion, τ_i, the compression ratio during the phase, $C_{i-1\,i}$, and the duration of the phase, Δt_i. These quantities are related by the equation

$$C_{i-1\,i} = (1 + \Delta t_i/\tau_i)^{-b_i}\,. \tag{3.22}$$

Thus, in order to describe a phase in the model, three of the four parameters need to be determined and the remaining one can be calculated from the above equation.

As defined in eqn (3.4), the compression ratio $C_{i-1\,i}$ is the ratio of the volume at the end of phase $(i-1)$ to the plasma volume at the end of phase i. It follows, then, that for an expansion phase the ratio is less than 1, while for a compression phase the ratio is greater than 1. The exponent b_i is related to the rate of the expansion or compression of the radio cocoon (see eqn (3.10)), while the time-scale τ_i is a characteristic time-scale of the expansion or the compression. Both of these quantities are determined by the physical process under which the volume of the plasma changes.

Extending eqn (3.12), the characteristic momentum of each phase is

$$p_{*\,i-1\,i} = \frac{C^{1/3}}{a_0 t_i \left(\frac{C^{5/3} - C^{1/b}}{1 - 5b/3} u_{\mathrm{B}\,i-1} + \frac{C^{1/3} - C^{1/b}}{1 - b/3} u_{\mathrm{C}} \right)}, \tag{3.23}$$

where to simplify the notation, $C = C_{i-1\,i}$ and $b = b_i$ and the time t_i is given by $t_i = \tau_i + \Delta t_i$. The magnetic energy density at the beginning of phase i is the same as that at the end of phase $(i-1)$:

$$u_{\mathrm{B}\,i-1} = u_{\mathrm{B}\,0}\,(C_{0\,i-1})^{4/3}. \tag{3.24}$$

Finally, combining the above equations, eqn (3.18) can be extended to give the resulting electron spectrum at the end of phase i:

$$N_i(p) = \tilde{N}_0\, C_{0\,i}^{\frac{s+2}{3}}\, p^{-s} \left(1 - \frac{p}{p_{*0\,i}}\right)^{s-2} \exp\left(- \left(\frac{p\, C_{0\,i}^{-\frac{1}{3}}}{p_c\,(1 - p/p_{*\,0\,i})} \right)^2 \right) \tag{3.25}$$

for $p_{\min i} = p_i(p_{\min 0}) < p < p_{\max i} = p_i(p_{\max 0})$ and $N_i(p) = 0$ otherwise. The electron spectrum shapes the resulting radio spectrum and hence, the radio spectrum is also determined at the end of each phase. The synchrotron emission of the radio cocoon at the end of phase i is given by

$$L_i(\nu) = \int_{p_{\min i}}^{p_{\max i}} \mathrm{d}p\, N_i(p) P_{\mathrm{sync}}(\nu, p), \tag{3.26}$$

where $P_{\mathrm{sync}}(p)$ is the synchrotron power of a single electron (see eqn (2.5)).

3.3 Discussion of the phases of the adiabatic compression model

The four phase parameters are determined through physical considerations of the active galaxy, the radio plasma and the thermal environment. However, some of the parameters for some phases are not determined by the model but are only fixed when applying the model to particular clusters and considering the cluster properties such as the shock strength and the pre-shock magnetic field. Below, the parameters for each phase, including which parameters need to be fixed by the physical conditions of the specific galaxy cluster to which the model is applied and which are free parameters, are discussed. This discussion closely follows the discussion in Enßlin & Gopal-Krishna (2001). The values of the parameters that are fixed within the model are listed in Table 3.1 for easy reference.

During phase 0, an active galaxy injects radio plasma into an expanding volume. The cocoon expands supersonically through a similar physical process as the expansion of AGN jets. Then, according to the formalism described by Kaiser & Alexander (1997), the volume changes according to a power-law with $b_0 = 9/5$ where the surrounding medium is assumed to have no density gradient. The expansion time-scale of the injection of the radio plasma is estimated from the typical age of a radio source at the end of its nuclear activity, giving $\tau_0 = 0.15$ Gyr (Alexander & Leahy, 1987; Enßlin & Gopal-Krishna, 2001). As this phase describes the conditions within the plasma after the nuclear activity of the galaxy has ceased, it has a duration of $\Delta t_0 = 0$ Gyr and similarly, the phase compression ratio is $C_{0\,0} = 1$.

After the galaxy activity has ceased, the cocoon is over-pressured with respect to the thermal surrounding (Begelman & Cioffi, 1989). As a result, the cocoon expands according to a Sedov-like expansion process where $b_1 = 6/5$ (Shu, 1992). As a simplification, the expansion is assumed to be Sedov-like until pressure equilibrium with the environment is reached. Momentum conservation implies that the expansion rate at the end of phase 0 and the start of phase 1 must be the same, leading to $\tau_1 = (b_1/b_0)\tau_0 = (2/3)\tau_0$ (Enßlin & Gopal-Krishna, 2001). For this phase, the compression ratio, $C_{0\,1}$, is constrained by the radio spectral index of the injected plasma and the pre-shock magnetic field of the cluster to which the model is applied. Then, the phase duration, Δt_1, is determined by eqn (3.22).

During phase 2, the cocoon is in pressure equilibrium with the environment. Hence the volume of the cocoon is largely constant, giving $C_{1\,2} \approx 1$ and $b_2 \approx 0$ from eqn (3.10). The time-scale of the expansion for this phase is $\tau_2 \to \infty$ (Enßlin & Gopal-Krishna, 2001). In this limit the maximal momentum (eqn (3.23)) of this phase is

$$p_{*1\,2} = \left[a_0 \left(u_{\mathrm{B}\,2} + u_{\mathrm{C}}\right) \Delta t_2\right]^{-1}. \tag{3.27}$$

Here, three of the four phase parameters are fixed, but since the expansion time-scale is infinite, the phase duration Δt_2 is not determined by eqn (3.22). Instead, for this phase the duration is a free parameter. However, since the electron population does experience radiative losses, the phase cannot last too long so that the radio emission of the revived plasma is still detectable.

The compression during phase 3 is due to the passage of the shock wave in the surrounding thermal gas as described by Enßlin & Gopal-Krishna (2001). The parameters b_3 and τ_3 are estimated by considering the process of the compression. As the shock wave moves past the radio cocoon, the cocoon is exposed to the high thermal pressure of the post-shock gas on its downstream side, while on its upstream side it is exposed to the ram-pressure of the pre-shock gas. However, since the remaining surface is only subject to the lower upstream gas pressure, the cocoon begins to expand orthogonally to the direction of the shock, taking on the typical arc-like morphology of radio relics. This behaviour is modelled by setting $b_3 = 2$ and a negative value for τ_3 determined from eqn (3.22). The phase duration is related to the volume of the plasma at the end of phase 2 and the pre-shock velocity in the shock frame:

$$\Delta t_3 = \frac{V_2^{1/3}}{v_{\mathrm{shock}\,2}}. \tag{3.28}$$

However, as it is difficult to estimate the volume of the radio plasma, it is easier to treat Δt_3 as a free parameter. Lastly, the phase compression ratio is estimated from the pressure jump, P_3/P_2, of the surrounding thermal gas, assuming pressure equilibrium before and after the shock passage:

$$C_{2\,3} = \left(\frac{P_3}{P_2}\right)^{3/4}, \tag{3.29}$$

where the pressure jump in thermal gas is related to the shock Mach number:

$$\frac{P_3}{P_2} = \frac{2\gamma\mathcal{M}^2}{\gamma+1} - \frac{\gamma-1}{\gamma+1}, \tag{3.30}$$

(Landau & Lifshitz, 1959) assuming the behaviour of a perfect gas. Here γ is the adiabatic index of the thermal gas: $\gamma = 5/3$.

Table 3.1: Summary of the values of each of the phase parameters as discussed in section 3.3. The values that are marked with a dash are determined from the cluster properties in each specific application.

Phase	Δt_i Myr	τ_i Myr	$C_{i-1\,i}$	b_i
0	0	15.0	1	1.8
1	$\left((C_{0\,1})^{-1/b_1} - 1\right)\tau_1$	10.0	< 1	1.2
2	—	∞	1	0
3	—	$\left((C_{2\,3})^{-1/b_3} - 1\right)^{-1} \Delta t_3 < 0$	$\left(\frac{P_3}{P_4}\right)^{3/4} > 1$	2
4	—	∞	1	0

During the final phase of the model, the radio plasma is once again in pressure equilibrium with the post-shock medium giving an expansion exponent of $b_4 = 0$ and a compression ratio of $C_{3\,4} = 1$ with a time-scale of expansion $\tau_4 \to \infty$ (Enßlin & Gopal-Krishna, 2001). As in phase 2, because the time-scale of expansion is infinite, the maximal momentum of the phase is given by eqn (3.27). The phase duration, Δt_4, is then not fixed by eqn (3.22) but is left as a free parameter that should be determined in each application of the model. However, since the electron population is losing energy very rapidly due to radiative losses, the phase duration strongly affects the level of radio emission produced by the relic.

3.4 The resulting radio spectrum

3.4.1 Relationship between the shock strength and the resulting radio spectrum

Since the fossil plasma is revived by the compression of the cocoon during the shock passage, the extent to which the cocoon is compressed will affect the shape of the resulting radio spectrum. As discussed above, the compression of the cocoon is related to the shock strength: as the shock Mach number increases, the compression of the phase increases (see eqns 3.29 and 3.30). Thus, a stronger shock should result in brighter radio emission of the relic as compared to the emission produced by a weak shock, as well as a flatter radio spectrum.

In order to investigate this relation between the shock strength and the radio spectrum of the revived plasma, the resulting radio spectrum was calculated for different values of the shock Mach number. A pre-shock magnetic field of $B_2 = 1.5\ \mu$G was used. The durations of phases 2 and 3 were kept constant at $\Delta t_2 = 2$ Myr and $\Delta t_3 = 10$ Myr, while the compression ratio of phase 1 was

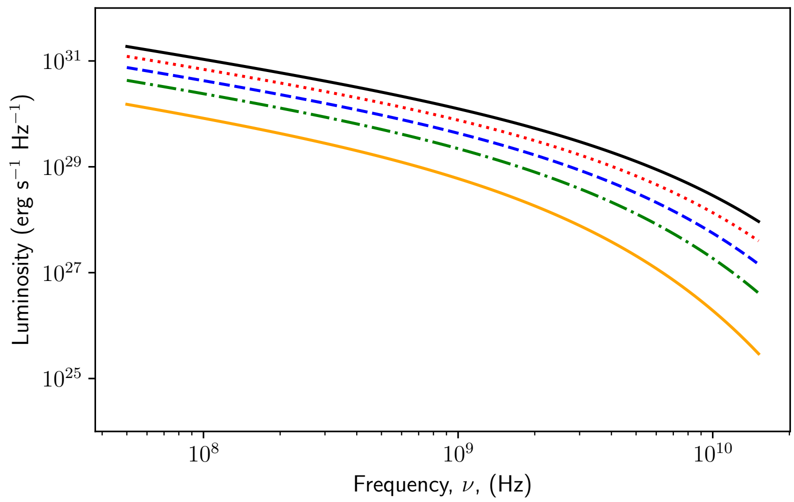

Figure 3.1: Resulting radio spectrum at the end of phase 3 showing that the spectrum flattens and the emission becomes brighter with increasing shock strength. The durations of phases 2 and 3 were fixed at $\Delta t_2 = 2$ Myr and $\Delta t_3 = 10$ Myr, respectively. The solid orange curve corresponds to a shock strength of $\mathcal{M} = 1.2$, the dot-dashed green curve to $\mathcal{M} = 1.5$, the dashed blue curve to $\mathcal{M} = 1.7$, the dotted red curve to $\mathcal{M} = 1.9$, and the solid black curve to $\mathcal{M} = 2.1$.

chosen to be $C_{01} = 0.6$. These values were chosen as reference values to be quite close to expected realistic values for clusters with a similar shock Mach number.

The resulting radio spectra are shown in Fig. 3.1. As expected, the radio luminosity of the relic after the shock passage increases with shock strength. Also, as seen in Table 3.2, the radio spectrum flattens as the shock Mach number increases. Relatively weak values of the shock strength were used ($1.5 \lesssim \mathcal{M} \lesssim 2.1$) here, yet the radio emission of the plasma after the shock passage only drops by 2 orders of magnitude, at most, over the whole frequency range. Furthermore, the resulting spectral indices of the revived plasma are in the range $-1.1 \lesssim \alpha \lesssim -1.6$ which is within the typical range of the spectral index of relics, $-1.0 \lesssim \alpha \lesssim -1.6$ (Feretti et al., 2012). This indicates that for appropriate values of the phase durations, Δt_2 and Δt_3, even a relatively weak shock can adequately revive fossil plasma under the adiabatic model.

3.4.2 Relationship between the phase durations and the resulting radio spectrum

As the volume during phase 2 remains largely constant, the only significant energy losses are the radiative losses, even though these losses are suppressed. Since these losses are irreversible, the longer the phase lasts, the more energy

Table 3.2: Resulting radio spectral index between 0.325 and 3.0 GHz as the shock strength is increased.

Shock Mach number	Spectral index
1.2	-1.57
1.5	-1.36
1.7	-1.27
1.9	-1.21
2.1	-1.15

the fossil plasma loses before being revived by the shock passage. Thus, the resulting radio spectrum of the cocoon after the shock passage will steepen as the duration of phase 2 increases.

This behaviour was investigated by calculating the radio spectrum at the end of phase 3 of the model for different phase durations, Δt_2. A shock Mach number of $\mathcal{M} = 1.7$ was used. The duration of phase 3 was kept constant at $\Delta t_3 = 10$ Myr and the compression ratio of phase 1 was, again, chosen to be $C_{0\,1} = 0.6$ with a pre-shock magnetic field of $B_2 = 1.5\ \mu$G.

Fig. 3.2 shows the resulting radio spectrum at the end of phase 3. As expected, the spectra clearly steepen as the duration of phase 2 increases. The emission of the revived plasma corresponding to a phase duration of $\Delta t_2 = 700$ Myr falls by about 4 or 5 orders of magnitude before 1 GHz (see the solid black curve in Fig. 3.2) showing that in this case the revived plasma is still very faint. This would indicate that for this shock strength and pre-shock magnetic field, the duration of phase 2 cannot be as much as 700 Myr in order to effectively revive the fossil plasma.

The effect of the duration of phase 3 on the resulting radio spectrum was also investigated. Again, the shock Mach number was kept constant at $\mathcal{M} = 1.7$ and the pre-shock magnetic field was chosen to be $B_2 = 1.5\ \mu$G. For the duration of phase 2 a value of $\Delta t_2 = 5$ Myr was used and the compression ratio of phase 1 was $C_{0\,1} = 0.6$.

This investigation shows that the maximum intensity of the luminosity that can be reached through the compression is given only by the shock strength (as shown by Fig. 3.1), while, for a given value of the Mach number, the luminosity steepens with the duration of the phase 3 due to the radiative losses (as shown in Fig. 3.3).

Phase 4 is dominated by heavy radiation losses as it describes the final fading away of the relic. Thus, the radio spectrum at the end of phase 4 should steepen as the duration of the phase increases. Using the same cluster properties and phase parameters as previously, the effect of increasing the duration of phase 4 on the shape of the radio spectrum was investigated. Fig. 3.4 shows the resulting spectra. As expected, the spectrum steepens with increasing phase duration, showing that the electron population is ageing.

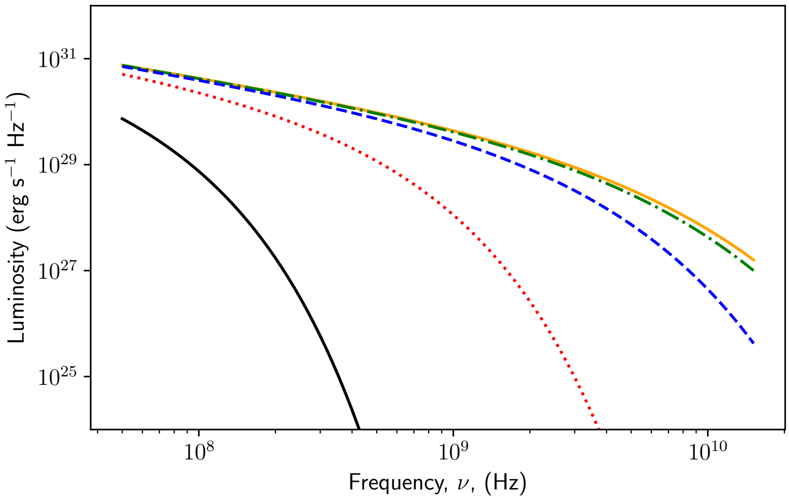

Figure 3.2: Resulting radio spectrum at the end of phase 3 showing that the radio spectrum steepens with the duration of phase 2 for a fixed shock strength of $\mathcal{M} = 1.7$ and a fixed duration of phase 3 of $\Delta t_3 = 10$ Myr. The solid orange curve corresponds to a duration of $\Delta t_2 = 1$ Myr, the dot-dashed green curve to $\Delta t_2 = 5.6$ Myr, the dashed blue curve to $\Delta t_2 = 32$ Myr, the dotted red curve to $\Delta t_2 = 180$ Myr, and the solid black curve to $\Delta t_2 = 700$ Myr.

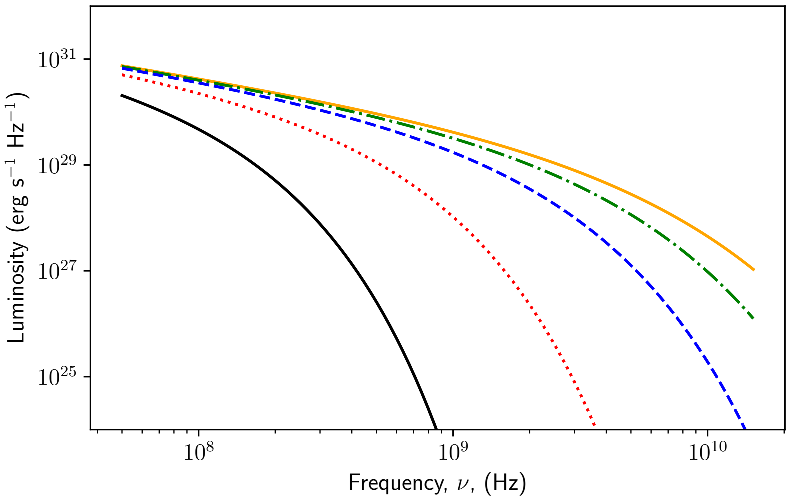

Figure 3.3: Resulting radio spectrum at the end of phase 3 showing that the radio spectrum steepens with the duration of phase 3 for a fixed shock strength of $\mathcal{M} = 1.7$ and a fixed duration phase 2 of $\Delta t_2 = 5$ Myr. The solid orange curve corresponds to a duration of $\Delta t_3 = 10$ Myr, the dot-dashed green curve to $\Delta t_3 = 30$ Myr, the dashed blue curve to $\Delta t_3 = 70$ Myr, the dotted red curve to $\Delta t_3 = 200$ Myr, and the solid black curve to $\Delta t_3 = 500$ Myr.

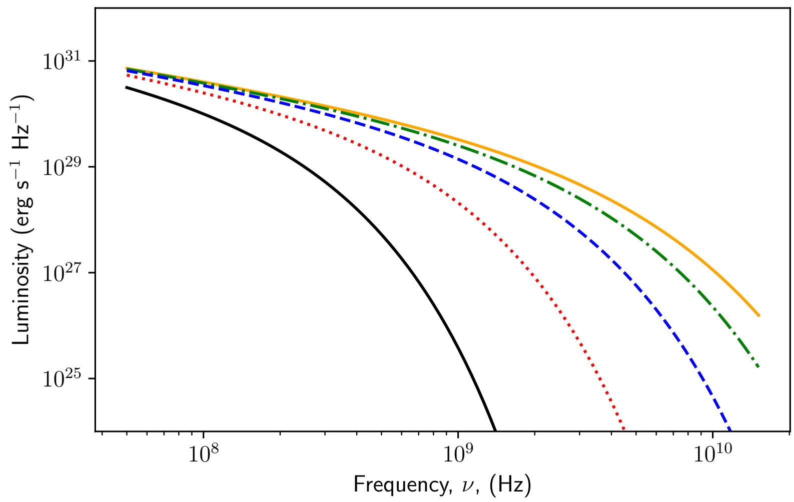

Figure 3.4: Resulting radio spectrum at the end of phase 4 showing that the radio spectrum steepens with the duration of phase 4. A fixed shock strength of $\mathcal{M} = 1.7$ and fixed durations of phases 2 and 3 of $\Delta t_2 = 5$ Myr and $\Delta t_3 = 10$ Myr were used. The solid orange curve corresponds to a duration of $\Delta t_4 = 10$ Myr, the dot-dashed green curve to $\Delta t_4 = 20$ Myr, the dashed blue curve to $\Delta t_4 = 40$ Myr, the dotted red curve to $\Delta t_4 = 90$ Myr, and the solid black curve to $\Delta t_4 = 200$ Myr.

3.5 Conclusion

This chapter presents the formalism of the adiabatic compression model. The model was also extended to describe the resulting radio spectrum of a more general electron population whose distribution follows a power-law with an exponential cut-off at high values of the dimensionless electron momentum, p.

The relationship between the shape of the resulting radio spectrum of the revived plasma and the shock strength was also investigated. As the shock strength increases, the radio spectrum flattens, indicating that the extent to which the fossil plasma is revived depends on the compression of the plasma which is determined by the shock strength. The calculations in this chapter were based on relatively weak shocks, $\mathcal{M} \lesssim 2.1$, however, the resulting radio emission after the shock passage drops by only 2 orders of magnitude over the frequency range used, and the resulting spectral indices are comparable to the expected spectral indices of radio relics.

Finally, the shape of the resulting radio spectrum for different durations of phases 2, 3, and 4 was investigated. Due to the radiative losses during the phase, the duration of phase 2 affects the shape of the radio spectrum at the end of phase 3: the longer phase 2 lasts, for a fixed shock strength, the steeper the radio spectrum at the end of phase 3. Thus, a weak cluster shock wave would require that the duration of phase 2 is fairly short, $\Delta t_2 \sim 10$ Myr, depending on the value of the spectral index at the position of the shock and the pre-shock magnetic field. During phase 3, radiative losses are still present and the longer the phase lasts, the more energy the radio plasma loses resulting in a steeper radio spectrum. Lastly, phase 4 is dominated by radiative losses as the emission of the plasma fades away and the duration of this final phase indicates the time-scale on which the source decays.

Chapter 4

Application of the adiabatic compression scenario to the relic hosted in A3411-3412

4.1 The radio relic hosted in the merging cluster A3411-3412

The galaxy cluster, A3411-3412, located at a redshift of $z = 0.162$, is currently undergoing a merging event of the two sub-clusters, A3411 and A3412, where the merger axis lies along the SE-NW direction (Van Weeren et al., 2013). The two merging clusters have similar masses ($\sim 10^{15}$ $M_{\odot}$ each) and are viewed about 1 Gyr after the first core passage (Van Weeren et al., 2017). The primary cluster came from the north but the lack of a surface brightness peak in the X-ray observations corresponding to the cluster core indicates that the core was disrupted during the collision with the southern sub-cluster. The sub-cluster A3411 came from the south and has a cometary shape with a well-defined sub-cluster core that has survived the collision until now (Van Weeren et al., 2013). From their X-ray observations, Van Weeren et al. (2013) calculated the global temperature of the merging cluster to be $6.4^{+0.6}_{-1.0}$ keV. The two merging galaxy sub-clusters, as well as the radio and X-ray emission of the cluster, are shown in Fig. 4.1.

Van Weeren et al. (2013) observed a region of diffuse radio emission to the south-east of the cluster centre along the major axis of the extended X-ray emission. This region is shown in Figs 4.2 and 4.3. They observed this region to be made up of five elongated components (which they labelled R1 to R5) with a total extent of 1.9 Mpc. From the size of the emission, its location with respect to the cluster centre, the lack of optical counterparts and its polarization properties, Van Weeren et al. (2013) classify this region as a radio relic. They identified three possible explanations for the complex morphology of the relic. Firstly, the morphology could result from the interaction of a

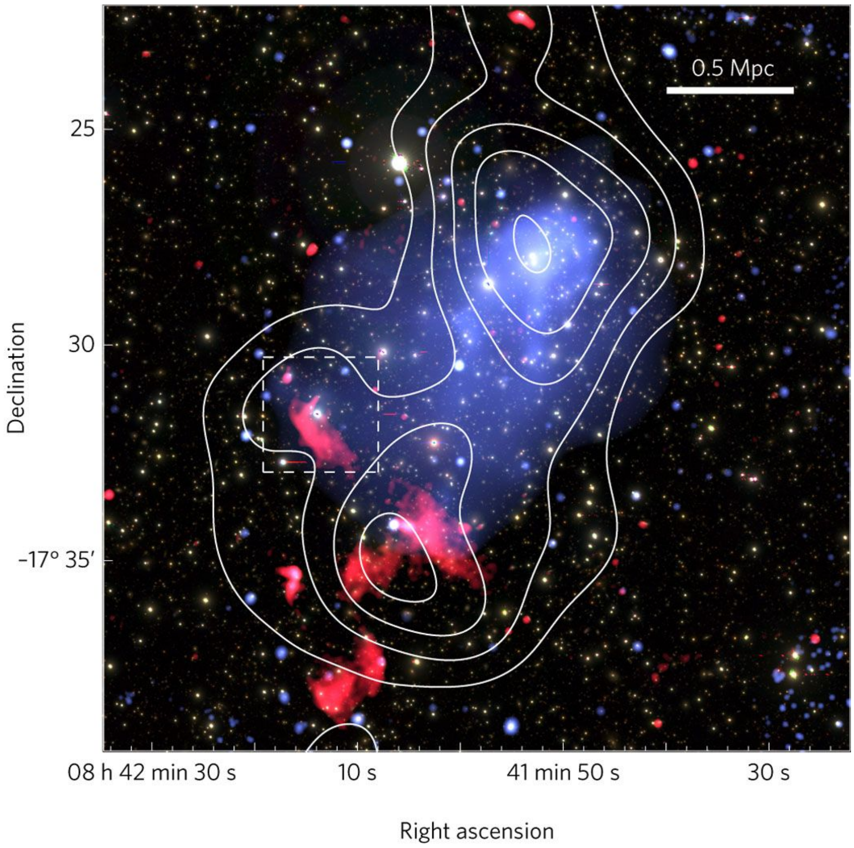

Figure 4.1: Subaru *gri* colour image of the merging cluster A3411-3412. Radio emission at 610 MHz from the GMRT is shown in red while the 0.5–3.0 keV image from *Chandra* is shown blue. Contour levels showing the galaxy distribution are drawn at $[3, 4, 5, \ldots]$ galaxies arcmin^{-2}. The region of the radio relic that is studied within this work is indicated by the dashed box (Van Weeren et al., 2017).

shock front with substructures or a large-scale galaxy filament from the cosmic web connected to the cluster. Secondly, the morphology could be caused by fluctuations in the magnetic field strength along the relic, caused by varying conditions along the shock front. And lastly, the complex morphology could result from the relativistic electrons being caught in several bubbles of fossil plasma due to previous AGN activity, which are then revived by the shock. Further observations by Giovannini et al. (2013) are consistent with the classification of this source as a radio relic, although their high-resolution images show that the morphology of the source is homogenous indicating that the whole source is likely to have a common origin. However, Van Weeren et al. (2017) found a cluster galaxy that is connected through a radio tail to the north-eastern portion of the relic (labelled R1 in Fig. 4.3) as well as two more galaxies (labelled A and B in Fig. 4.3), one of which has a tail of steep spectrum emission extending towards the relic and the other is embedded within the relic emission, suggesting that all the components of the complex relic trace revived fossil plasma.

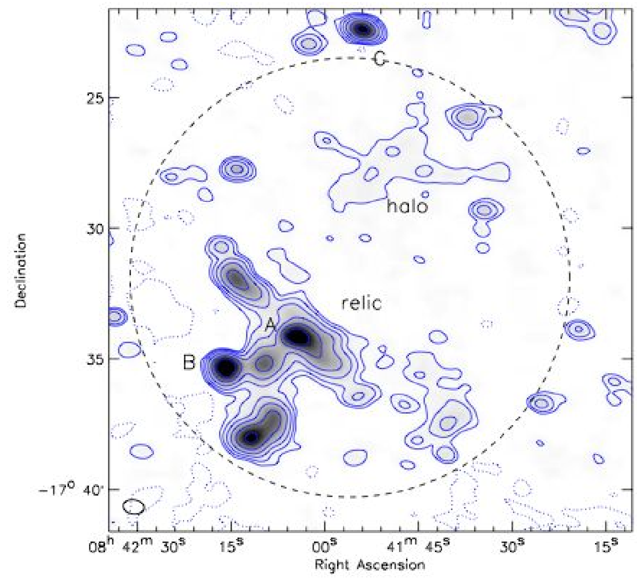

Figure 4.2: Radio image showing the central halo and the relic hosted in A3411-3412 taken with the VLA at 1.4 GHz in the DnC array configuration with a beam size of $48'' \times 33''$. Contour levels are drawn at $[1, 2, 4, 8, \ldots] \times 3\sigma_{\rm rms}$, where $\sigma_{\rm rms} = 47$ μJy beam^{-1}, and $-3\sigma_{\rm rms}$ contours are shown by dotted lines (Van Weeren et al., 2013). The dashed circle indicates the region where Van Weeren et al. (2013) extracted fluxes for their paper.

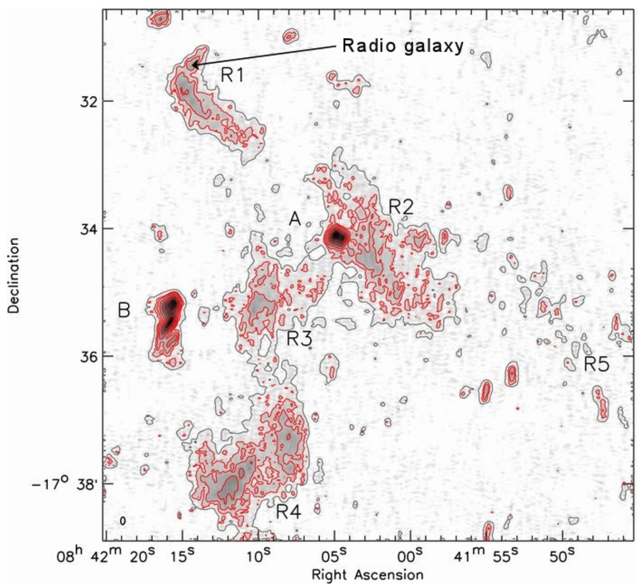

Figure 4.3: Radio image of the radio relic in the SE region of the cluster A3411-3412 taken with the VLA at 1.4 GHz in the BnA array configuration. The five elongated components of the relic are labelled R1 to R5. The north-eastern component of the relic that is connected to a cluster galaxy is labelled R1. Contour levels in red are drawn at $[1, 2, 4, 8, \ldots] \times 4\sigma_{\rm rms}$, where $\sigma_{\rm rms} = 15$ μJy beam^{-1}, and the grey contours are drawn at $1.5\sigma_{\rm rms}$ using a boxcar average of $7''$. The beam size is shown at the bottom left corner of the image (Van Weeren et al., 2013).

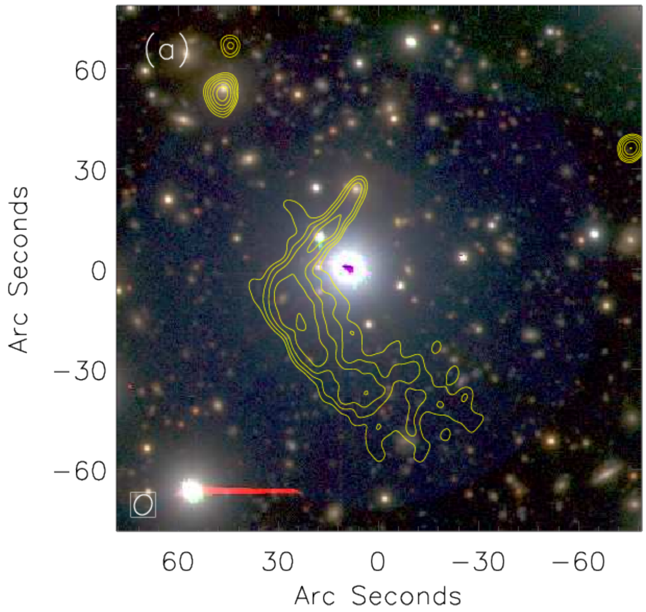

Figure 4.4: Subaru optical *gri* colour image of the NE component of the radio relic showing the radio tail connecting the relic to the radio galaxy. The yellow overlaid contours are from the GMRT 610 MHz observations and the contour levels are drawn at $\sqrt{[1, 2, 4, \ldots]} \times 5\sigma_{\mathrm{rms}}$. The beam size is shown in the bottom left corner (Van Weeren et al., 2017).

From their X-ray observations Van Weeren et al. (2017) detected a shock front at the relic's outer edge. This is consistent with the understanding that radio relics trace shock fronts (Enßlin et al., 1998). The X-ray surface brightness profile indicates that the shock is rather weak with a Mach number of $1.2 \lesssim \mathcal{M} \lesssim 1.7$. However, this derivation of the shock Mach number is based on a broken power-law density model and the assumptions of the projection effects and shock geometry might be incorrect, which could result in an underestimation of the shock Mach number. Because temperature measurements are less affected by an unknown geometry, a better method of determining the shock Mach number is to use the temperature discontinuity. However, this method is not possible in this case, since there are no meaningful constraints on the pre-shock X-ray gas temperature (Van Weeren et al., 2017).

In a head-on merger event of a binary cluster, two shocks propagating outwards are expected to form along the merger axis (Roettiger et al., 1999). However, Van Weeren et al. (2013) did not find any evidence of a second radio relic in the region to the north-west of the sub-cluster core. This could indicate that the counter-shock is not strong enough to efficiently accelerate particles, that there is a lack of pre-accelerated fossil electrons that could be re-accelerated by the shock, or that the relic emission is detected but it is very faint and indistinguishable from the halo emission (Van Weeren et al., 2013).

This work focuses on the north-eastern component of the relic (labelled R1 by Van Weeren et al. (2013)) that was studied previously by Van Weeren et al.

Table 4.1: Flux densities at 0.325, 0.610, 1.5 and 3.0 GHz measured at intervals of 20 kpc across the relic (Van Weeren et al., 2017).

Distance kpc	$F_{0.325}$ μJy	$F_{0.610}$ μJy	$F_{1.5}$ μJy	$F_{3.0}$ μJy
40	—	—	58.8	—
60	1620	735	618	294
80	5710	3120	1410	706
100	5940	3240	1120	471
120	3470	1940	647	118
140	2180	1060	412	—
160	1240	412	235	—
180	529	353	—	—
200	—	176	—	—

(2017) and is shown in Fig. 4.4. The radio tail connecting the relic to the cluster galaxy could be a source of radio plasma and the presence of a shock at the position of the relic provides a way for the fossil plasma to be re-energized. This work investigates a scenario where this portion of the relic is formed from fossil plasma that was injected by the galaxy and then revived through adiabatic compression caused by the passage of the merger shock. The aim of the project is, therefore, to use the adiabatic model to reproduce the spectral index of the relic immediately behind the shock front.

Since the radio plasma is revived by the shock wave, the position with the greatest flux density should correspond to the position of the shock. In front of the shock, the plasma is still to be revived and so it should have a steeper spectrum and lower radio emission compared to the emission at the position of the shock, while the plasma behind the shock loses energy rapidly due to radiative emission and so would also have a steeper spectrum and lower radio emission. Van Weeren et al. (2017) measured the flux density at intervals of 20 kpc across the relic. Their flux density profiles across the relic are shown here in Fig. 4.5 and the flux density values are listed in Table 4.1. The position of the shock front is taken to be between 80 and 100 kpc, in accordance with these observations. It is interesting to note that the flux densities measured at the higher frequencies (1.5 and 3.0 GHz) reach a peak value at 100 kpc while the flux densities at the lower frequencies (325 and 610 MHz) reach a peak value at 80 kpc. This makes it difficult to determine the exact position of the shock front.

According to the results found by Van Weeren et al. (2017), the spectral index between 0.325 and 3.0 GHz of the radio tail connecting the relic to the cluster galaxy steepens from $\alpha = -0.5 \pm 0.1$ at the galaxy nucleus to $\alpha = -1.3 \pm 0.1$ at the end of the radio bridge which is consistent with synchrotron and inverse Compton losses. However, at the position where the radio plasma from the galaxy joins the relic, the spectral index flattens to $\alpha = -0.9 \pm 0.1$. The spectral

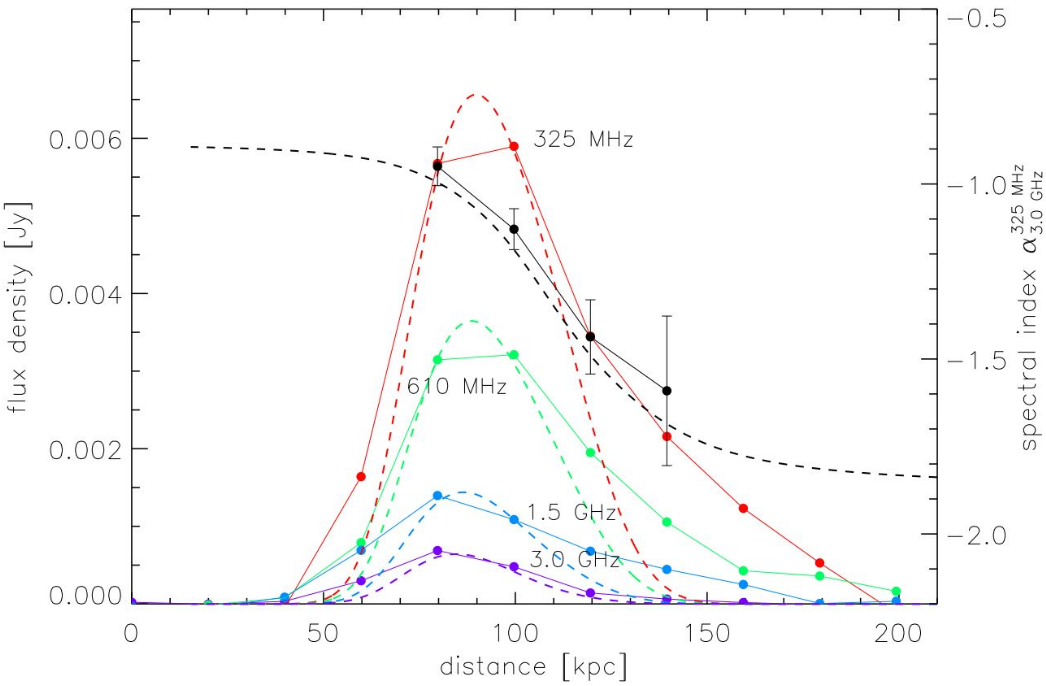

Figure 4.5: Measured flux density profiles across the width of the north-eastern component of the radio relic in A3411-3412. The flux densities measured at 325 MHz are shown in the red points series, those measured at 610 MHz are shown in the green point series, those measured at 1.5 GHz are shown in the blue point series and those measured at 3.0 GHz are shown in the purple point series. The solid coloured lines connect the data points at the respective frequency while the dashed coloured lines are modelled profiles from the DSA-type re-acceleration model. The spectral indices between 325 MHz and 3.0 GHz across the relic are shown in black, where the solid lines connect the data points and the dashed black line is the spectral index profile that results from the DSA-type re-acceleration model. Uncertainties are plotted at the 1σ level (Van Weeren et al., 2017).

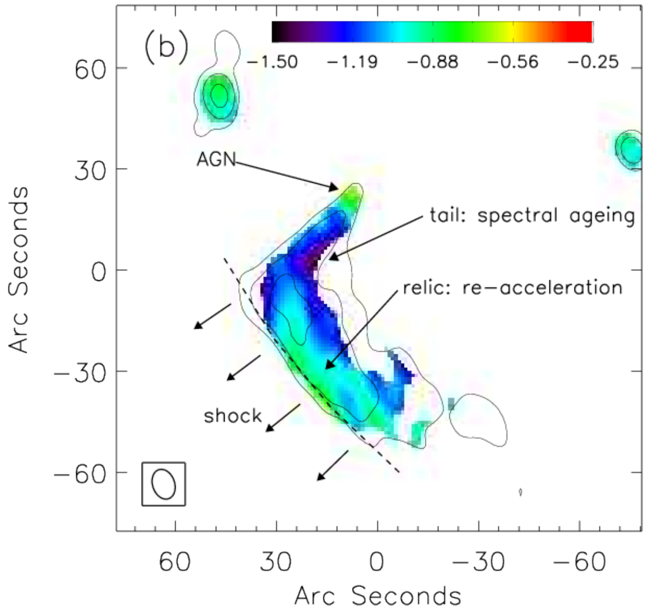

Figure 4.6: Radio spectral index map of the north-eastern component of the radio relic in A3411-3412. The spectral index was determined using matched observations at frequencies 0.310, 0.625, 1.5, and 3.0 GHz. The overlaid contours from the 0.325 GHz GMRT image are drawn at levels of $[1, 2, 4, \ldots] \times 6\sigma_{\mathrm{rms}}$. The best-fitting position of the X-ray surface brightness edge is indicated by the black dashed line. The size is indicated in the bottom left-hand corner (Van Weeren et al., 2017).

Table 4.2: Measured spectral indices between 0.325 and 3.0 GHz at four points across the relic where the distance is measured from a point on the edge of the relic towards the cluster centre (Van Weeren et al., 2017).

Distance / kpc	Spectral index
80	−0.953
100	−1.12
120	−1.42
140	−1.59

index along the length of the relic remains largely flat, although it steepens across the relic towards the cluster centre. The same authors measured the spectral index between 0.325 and 3.0 GHz at four points across the relic and their results are shown here in Fig. 4.5. The spectral index map showing the relatively flat spectrum along the relic and the steepening towards the centre is also shown here in Fig. 4.6. For comparison with the results in this work, the values of the measured spectral indices are listed in Table 4.2.

4.2 Method

As discussed in chapter 3, several of the model parameters for each phase need to be determined in each application of the model. Some of these parameters are free parameters that are chosen to obtain the best-fitting values of the spectral index at the end of each phase. It is then necessary to determine the values of the spectral index across the relic that correspond to each phase of the adiabatic model.

The compression ratio of phase 3 is determined from the value of the shock Mach number which was taken to be $\mathcal{M} = 1.7$, according to the upper limit obtained by Van Weeren et al. (2017). From this value, the compression ratio of phase 3 is calculated from eqns (3.29) and (3.30) to be $C_{2\,3} = 2.48$.

Phase 3 of the adiabatic model describes the action of the shock front to revive the fossil plasma. Therefore, the spectral index at the end of this phase should correspond to the spectral index at the position of the shock front. As discussed above, the exact position of the shock front is difficult to determine, but the flattest measured value of the spectral index is -0.953 and occurs at 80 kpc. This modelling, therefore, attempts to fit the spectral index at the end of phase 3 to this value. Of the values of the spectral index across the relic that are available, the value of -1.59 that occurs at 140 kpc is the one that is furthest from the shock front. Thus, the value of the spectral index at the end of phase 4 is matched to this value. Since the initial electron population is injected by the radio galaxy, the spectral index at the end of phase 0 is matched to the value of the spectral index of the galaxy, -0.5. The electron cloud at the end of the radio tail corresponds to the electron population at the end of phase 2 before the action of the compression caused by the shock passage. Thus, the desired spectral index at the end of phase 2 corresponds to the spectral index at the point of conjunction between the radio tail and the radio relic, shown in Fig. 4.6, which is -1.3 (Van Weeren et al., 2017, see also chapter 2). The value of the spectral index at the end of phase 1 is not constrained; however, due to the expansion during this phase it will be steeper than the spectral index at the end of phase 0. The expected spectral index for each phase is listed in Table 4.3. The values of the free parameters, $C_{0\,1}$, Δt_2, Δt_3, and Δt_4, were varied until the calculated spectral indices at the end of each phase matched these spectral indices across the relic. The values of Δt_1 and τ_3 are calculated from the values of $C_{0\,1}$ and Δt_3 according to eqn (3.22).

Finally, the cosmic microwave background (CMB) radiation field energy density, u_{C}, is given by the blackbody radiation density where the temperature depends on the redshift of the galaxy cluster, according to the equation

$$u_{\mathrm{C}} = \frac{4\sigma T^4}{c} = \frac{4\sigma(2.725(1+z))^4}{c}. \tag{4.1}$$

Thus, for the redshift of the cluster galaxy connected to the radio tail, $z = 0.164$, (Van Weeren et al., 2017), the corresponding CMB radiation field energy density is $u_{\mathrm{C}} = 7.66 \times 10^{-13}$ erg cm^{-3} or $u_{\mathrm{C}} = 0.478$ eV cm^{-3}.

Table 4.3: Expected values of the spectral index at the end of each phase.

Phase	Spectral index
0	−0.5
1	Not specified
2	−1.3
3	−0.95
4	−1.6

The value used for the pre-shock magnetic field strength was the same as that used in the modelling performed by Van Weeren et al. (2017): $B = 1.5\ \mu$G. In this model, the pre-shock magnetic field corresponds to the magnetic field of phase 2. From this value, the values of the magnetic field in the other phases of the adiabatic model were calculated according to eqn (3.24) where the magnetic field energy density and the magnetic field strength are related by

$$u_{\mathrm{B}} = \frac{1}{8\pi} B^2, \tag{4.2}$$

in CGS units.

The electron spectrum at the end of the radio tail was studied in chapter 2 where it was shown that it can be described by the equation

$$N(p) = \tilde{N}\, p^{-2.5} \exp\left(-(p/p_c)^2\right), \tag{4.3}$$

where p is the dimensionless momentum of an electron and $p_c = 1.8 \times 10^4$. The value of the normalization was calculated in chapter 2 to be $\tilde{N} = 1.1 \times 10^{63}$ for a magnetic field of 1.5 μG. As shown in chapter 2, the resulting radio spectrum of this electron population is −1.3. However, the electron spectrum of the galaxy is not easily determined since the magnetic field and the flux density of the galaxy are unknown. Because of this difficulty, this study first examined the case where the electron spectrum at the end of phase 2 was given by eqn (4.3) and where the evolution of the electron spectrum was followed from this point on.

The study was then extended to investigate the full evolution of the electron spectrum under all the phases of the adiabatic model. The injection spectrum was found by estimating the electron spectrum of the galaxy. The radio spectrum of −0.5 is best reproduced by a pure power-law spectrum with a slope of −2:

$$N_0(p_0) = \tilde{N}_0 p^{-2}. \tag{4.4}$$

Since the magnetic field and the flux density of the galaxy are unknown, the constant $\tilde{N}_0$ was estimated by matching the calculated flux density at the end of phase 3 with the peak flux density of the relic. The best-fitting value is $\tilde{N}_0 = 2.2 \times 10^{61}$. The electron spectrum at the end of each phase of the adiabatic model is then calculated according to the formalism of the adiabatic compression model (Enßlin & Gopal-Krishna, 2001).

Using the values of these parameters, the evolution of the electron population was determined at the end of each phase of the model according to eqn (3.25). From these electron spectra, the luminosity and flux density at the end of each phase were calculated from eqns (3.26) and (2.7), respectively.

4.3 Results and discussion

This section considers four different scenarios in which the adiabatic compression model is applied to the radio relic hosted in A3411-3412. In the first scenario, the electron spectrum at the end of phase 2 is assumed to be given by the spectrum at the end of the radio tail, and the evolution of the spectrum is followed from this point on. The other three scenarios all study the evolution of the electron spectrum through all the phases of the adiabatic model starting with the injection of the electron population by the radio galaxy. These scenarios differ from each other in the assumptions made regarding the duration or expansion of the fourth phase of the model. A comparison of the resulting radio spectral indices between 0.325 and 3.0 GHz for the four cases is presented in Table 4.8.

4.3.1 Scenario 1: Evolution of the electron spectrum during the last three phases of the adiabatic model

In this scenario, it is assumed that the electron spectrum at the end of phase 2 is fixed and is given by the electron spectrum at the end of the radio tail as described by eqn (4.3). The radio tail joins the radio galaxy to the arc-shaped radio relic, which indicates that this region of emission could represent the emission that is produced during phase 2 of the adiabatic model. As mentioned above, the electron spectrum of this region was studied in chapter 2 and can be well described by eqn (4.3). Since phases 3 and 4 are directly related to the relic formation, this scenario was chosen so as to simplify the approach to studying the relic formation.

Since, in this scenario, the second phase of the model is treated as the initial phase and the electron spectrum at the end of the phase is assumed to be known, the duration of phase 2 was taken to be 0 Myr. The duration of phase 3, Δt_3, was chosen to produce the flattest spectral index in an attempt to match the spectral index at the end of the phase to the measured value at 80 kpc. The best-fitting value was found to be 0.1 Myr; however, it was found that even a small value of Δt_3 could not reproduce the spectral index at 80 kpc very well. The resulting value of τ_3 was -0.273 Myr. Finally, the duration of phase 4 that reproduced the spectral index at 140 kpc was found to be $\Delta t_4 = 26$ Myr. These values of the parameters as well as the resulting magnetic field values and the characteristic momenta are listed in Table 4.4. The radio spectra calculated from these values are shown in Fig. 4.7.

Table 4.4: Best-fitting values of the phase parameters used in scenario 1 and the calculated cumulative compression ratios, magnetic field values, magnetic energy densities and characteristic momenta. The columns are grouped according to the phase parameters and the quantities that are calculated from the phase parameters.

Phase	Δt_i Myr	τ_i Myr	$C_{i-1\,i}$	b_i	$C_{0\,i}$	B_i μG	$u_{B\,i}$ eV cm^{-3}	$p_{*0\,i}$
2	0	∞	1	0	1	1.50	0.0559	∞
3	0.1	-0.274	2.48	2	2.48	2.75	0.188	12 200 000
4	26	∞	1	0	2.48	2.75	0.188	25 900

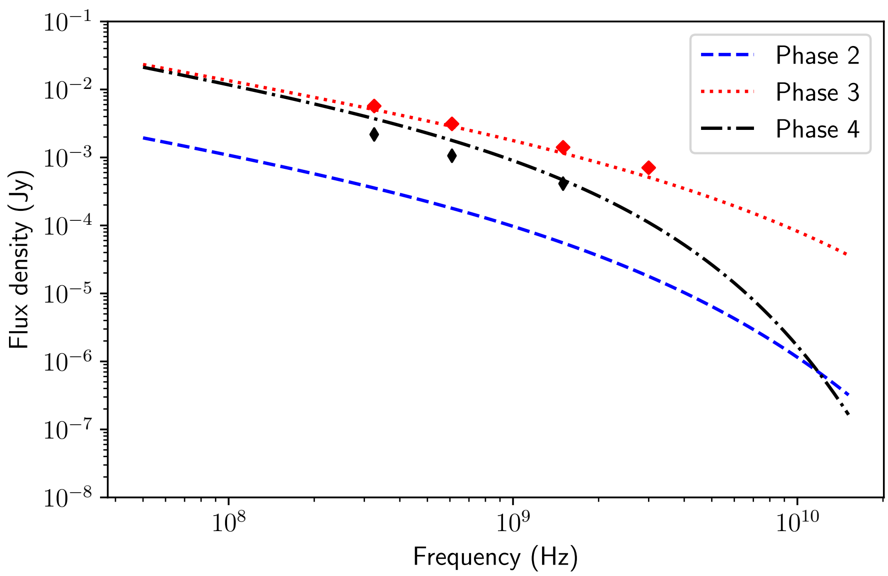

Figure 4.7: Flux densities from the scenario 1 modelling, where the electron spectrum at the end of the radio tail was taken as the electron spectrum at the end of phase 2. Model results at the end of phases 2, 3 and 4 are shown. The measured flux densities at 80 kpc and 140 kpc are shown in the red and black point series, respectively.

The resulting radio spectrum at the end of phase 3 (shown by the dotted red curve in Fig. 4.7) seems to fit the measured flux density at 80 kpc, although the spectrum is steeper than the measured spectrum. The calculated spectral index between 0.325 and 3.0 GHz at the end of phase 3 is −1.03, whereas the measured spectral index at 80 kpc is −0.95. As noted above, decreasing the value of Δt_3 did not produce a significantly flatter spectrum. The slope of the electron population or the value of the exponential cut-off would change the shape of the spectrum significantly. However, given that there is some uncertainty as to the position of the shock front, this result is still promising. Lastly, the calculated radio spectrum at the end of phase 4 lies above the measured spectrum at 140 kpc, even though the model does reproduce the measured spectral index of −1.58 as shown in Table 4.8.

The results of this scenario, which only considered the final stages of the model, demonstrate that the adiabatic model could be successful in describing the formation of this relic. It is, therefore, worthwhile to consider the application of the full model and to investigate whether it could be more successful at reproducing the radio spectrum at the position of the shock front than this scenario.

4.3.2 Scenario 2: Application of the full adiabatic model

In this scenario, the electron population is injected by the radio galaxy to the north of the relic and the initial electron spectrum is assumed to be given by eqn (4.4). This electron spectrum is flatter than the spectrum considered in the scenario above and is a pure power-law rather than a power-law with an exponential cut-off. This should be able to produce a flatter radio spectrum at the end of phase 3.

The value of the compression ratio of phase 1 was chosen to produce the best-fitting values of the spectral indices of phase 0 and phase 2; the resulting value was $C_{0\,1} = 0.7$. The resulting duration of phase 1 was then calculated to be $\Delta t_1 = 3.46$ Myr. The durations of phases 2 and 3 that best reproduce the spectral indices at the end of the radio tail and at the shock front were found to be 54 Myr and 2.5 Myr, respectively, with the resulting value of τ_3 calculated to be −6.84 Myr. Lastly, the duration of phase 4 that reproduces the spectral index at 140 kpc is 28 Myr. The best-fitting model values are listed in Table 4.5 and the resulting radio spectra are shown in Fig. 4.8.

This scenario is successful in reproducing the measured flux density at the position of the shock front. The calculated spectrum at the end of phase 3, shown by the dotted red curve in Fig. 4.8, clearly follows the shape of the measured spectrum at 80 kpc. This is confirmed by considering the radio spectral index, as the calculated value of −0.954 matches the measured value of −0.95. Furthermore, the curve also fits the measured flux density at this position. This is expected since the normalization of the electron population

Table 4.5: Best-fitting values of the phase parameters used in scenario 2 and the calculated cumulative compression ratios, magnetic field values, magnetic energy densities and characteristic momenta. The columns are grouped according to the phase parameters and the quantities that are calculated from the phase parameters.

Phase	Δt_i Myr	τ_i Myr	$C_{i-1\,i}$	b_i	$C_{0\,i}$	B_i μG	$u_{\mathrm{B}\,i}$ eV cm^{-3}	$p_{*0\,i}$
0	0	15.0	1	1.8	1.0	1.90	0.0899	∞
1	3.46	10.0	0.7	1.2	0.70	1.50	0.0559	303 000
2	54	∞	1	0	0.70	1.50	0.0559	22 100
3	2.5	−6.84	2.48	2	1.74	2.75	0.188	21 200
4	28	∞	1	0	1.74	2.75	0.188	11 900

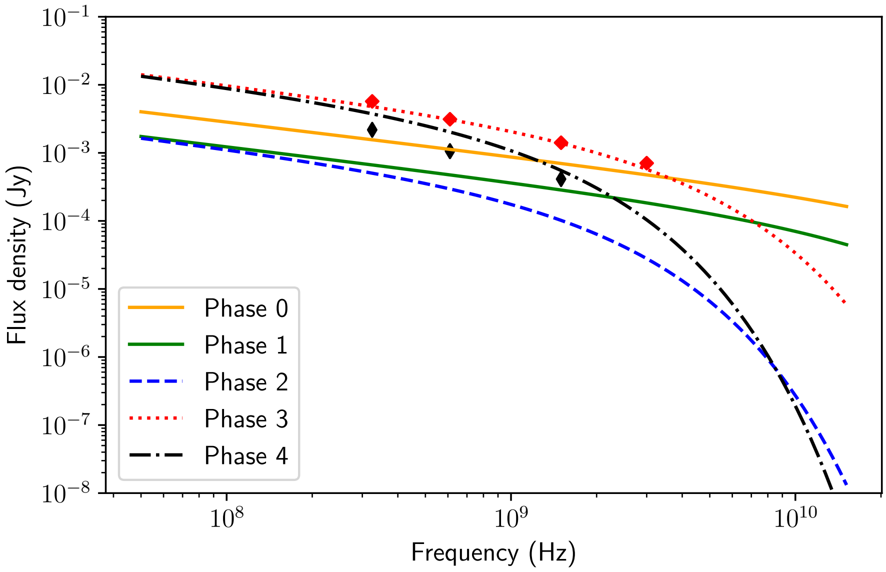

Figure 4.8: Flux densities from the scenario 2 modelling, where the electron population was injected by the radio galaxy and the evolution of the electron spectrum is studied through all the phases of the adiabatic model. The measured flux densities at 80 kpc and 140 kpc are shown in the red and black point series, respectively.

was chosen by fitting the flux density at this position. The observations of the relic, as shown in the radio maps in Van Weeren et al. (2017), indicate that the emission of the galaxy is weaker than the peak emission of the relic. Thus, since the calculated spectrum at the end of phase 0 (shown in the solid orange curve) is below the peak emission of the relic, this value of the normalization is reasonable.

Finally, as in the previous case, the radio spectrum at the end of phase 4, shown by the dot-dashed black curve in Fig. 4.8, lies above the measured radio spectrum at 140 kpc even though it has the same spectral shape. This indicates that further investigation of the radio spectrum behind the shock front is required. The next two scenarios investigate this problem.

4.3.3 Scenario 3: Investigation of a steeper spectrum behind the shock front

As the previous scenario demonstrates, the full adiabatic model is able to reproduce the spectral shape of the radio emission at the shock front, although there seems to be some difficulty in recovering the flux density at the measured radio spectral index at 140 kpc. This and the scenario in section 4.3.4 investigate two different methods to try and resolve this difficulty. In this scenario, as in the previous one, the injection electron spectrum is assumed to be given by eqn (4.4) and the evolution is followed through all the phases of the model. However, here the radio spectrum behind the shock front was allowed to be steeper than the measured spectral index at 140 kpc and the calculated spectrum was matched to the flux density rather than the spectral shape. Since phase 4 describes the final fading away of the relic, it is difficult to find the position of the emission that should correspond to this phase and it makes sense to explore regions of emission further away from the shock front. The calculated spectrum was, therefore, also compared with the flux density and spectral shape of the measured spectrum at 160 kpc.

The values of all the phase parameters before phase 4 were chosen in the same way as in the previous case. The duration of phase 4 was chosen as the value that best reproduced the flux density at 140 kpc. The best-fitting value was found to be 50 Myr. The phase parameters are listed in Table 4.6 and the resulting radio spectra are shown in Fig. 4.9.

The longer duration of phase 4 in this scenario compared to that in scenario 2 in section 4.3.2, produces a lower flux density. This is expected since the longer the duration of this phase the more the radiative losses and so the lower the flux density. As shown by the solid black curve in Fig. 4.9, the calculated spectrum fits the measured flux density at 325 and 610 MHz but lies below the measured flux density at 1.5 GHz.

The calculated spectrum at the end of phase 4 was also compared to the measured spectrum at 160 kpc and is shown together with the data at both 140

Table 4.6: Best-fitting values of the phase parameters used in scenario 3 and the calculated cumulative compression ratios, magnetic field values, magnetic energy densities and characteristic momenta. The columns are grouped according to the phase parameters and the quantities that are calculated from the phase parameters.

Phase	Δt_i Myr	τ_i Myr	$C_{i-1\,i}$	b_i	$C_{0\,i}$	B_i μG	$u_{\mathrm{B}\,i}$ eV cm^{-3}	$p_{*0\,i}$
0	0	15.0	1	1.8	1.0	1.90	0.0899	∞
1	3.46	10.0	0.7	1.2	0.70	1.50	0.0559	303 000
2	54	∞	1	0	0.70	1.50	0.0559	22 100
3	2.5	−6.84	2.48	2	1.74	2.75	0.188	21 200
4	50	∞	1	0	1.74	2.75	0.188	8 860

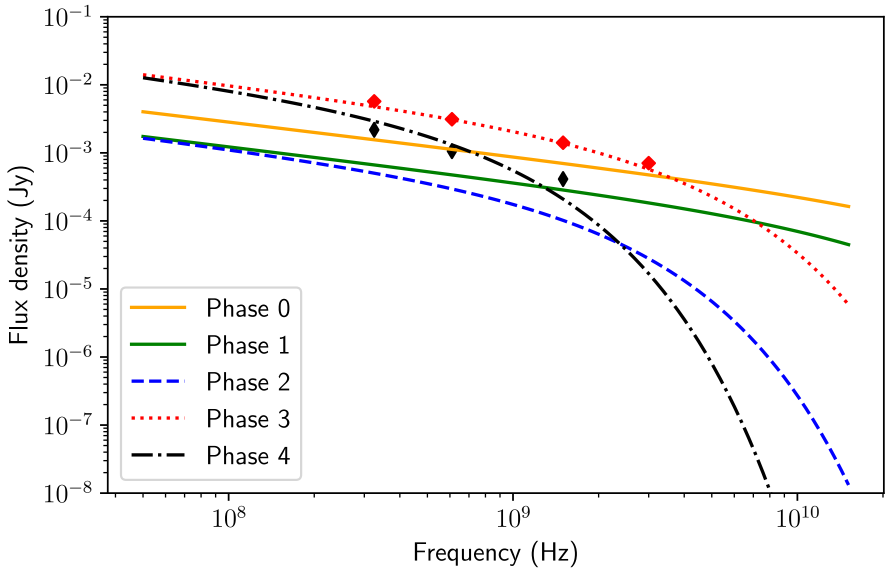

Figure 4.9: Flux densities from the scenario 3 modelling where the duration of phase 4 was increased to produce a steeper spectrum behind the shock front. The radio spectra at the end of each phase of the model are shown. The flux densities at 80 kpc and 140 kpc are shown in the red and black point series, respectively.

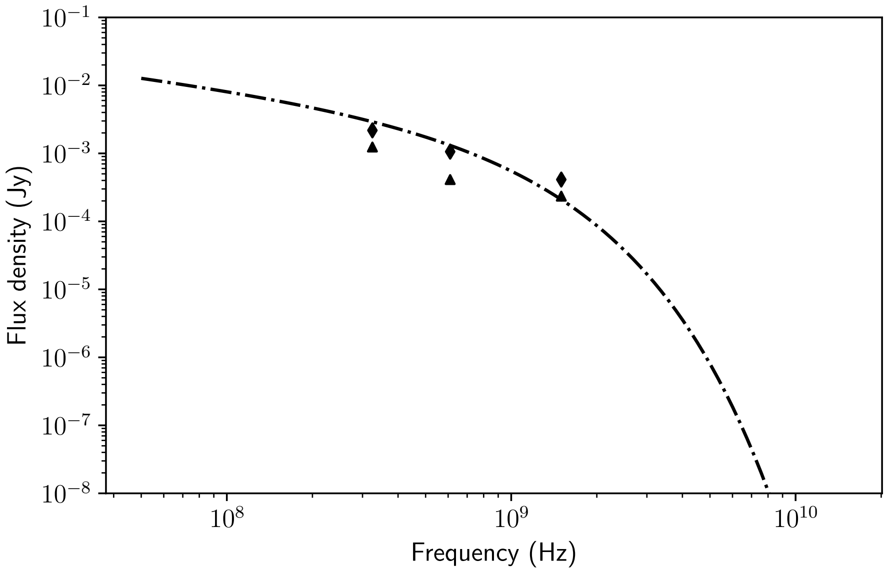

Figure 4.10: Comparison of the flux density at the end of phase 4 calculated in scenario 3 to the measured flux densities at both 140 kpc and 160 kpc. The flux density at the end of phase 4 is shown by the black dot-dashed curve, while the measured flux densities at 140 kpc are shown by the black diamonds and the measured flux densities at 160 kpc are shown by the black triangles. The flux densities of the other phases are as shown in Fig. 4.9

kpc and 160 kpc in Fig. 4.10. This figure shows that the calculated spectrum lies above the flux density at 325 and 610 MHz measured at 160 kpc but passes through the point at 1.5 GHz, indicating that it is difficult to reproduce the flux density at all three frequencies by considering only the radiative energy losses.

Furthermore, the comparison of the data at 140 kpc and 160 kpc seems to indicate that the flux density at 1.5 GHz seems to decrease more slowly with distance behind the shock front than the flux density at lower frequencies. This could indicate that other mechanisms, such as turbulence (Fujita et al., 2015), are effective behind the shock front and continue to energize the electrons in this region. Another possibility is that the radio cocoon starts to expand slightly after the shock passage, so that the energy losses at the higher frequencies are less rapid than at the lower frequencies producing a flatter radio spectrum. The effect of such a mechanism is investigated in section 4.3.4.

4.3.4 Scenario 4: Investigation of an expansion phase behind the shock front

The previous scenario demonstrates that it is difficult to match the flux density at both the low frequency and high frequency at the same time by consider-

Table 4.7: Best-fitting values of the phase parameters used in scenario 4 and the calculated cumulative compression ratios, magnetic field values, magnetic energy density and characteristic momenta. The columns are grouped according to the phase parameters and the quantities that are calculated from the phase parameters.

Phase	Δt_i Myr	τ_i Myr	$C_{i-1\,i}$	b_i	$C_{0\,i}$	B_i μG	$u_{\mathrm{B}\,i}$ eV cm^{-3}	$p_{*0\,i}$
0	0	15	1	1.8	1.0	1.90	0.0899	∞
1	3.46	10.0	0.7	1.2	0.70	1.50	0.0559	303 000
2	54	∞	1	0	0.70	1.50	0.0559	22 100
3	2.5	−6.84	2.48	2	1.74	2.75	0.188	21 200
4	22	88.0	0.8	1	1.39	2.37	0.140	13 200

ing only radiative energy losses. This scenario investigates the effects of an expansion of the radio cocoon following the compression caused by the shock passage. Physically, it could be possible that after the cocoon is compressed by the shock passage, it is over-pressured compared to the environment and starts to expand. This effect is probably quite small and the rate of expansion is probably smaller than that for phase 1.

As in the last two scenarios, this scenario follows the evolution of the electron spectrum through all the phases of the model and the initial electron spectrum is assumed to be given by eqn (4.4). Again, the values of the phase parameters until phase 4 were chosen in the same way as in scenario 2 in section 4.3.2. The parameters of phase 4 were chosen to give the best-fitting results for both the flux density and the spectral index without working out a physical model of the expansion. The compression ratio, $C_{3\,4}$ was chosen to be 0.8 since this represents an expansion of the cocoon but is still close to one. The exponent of the expansion, b_4, was chosen to be 1 which would correspond to an expansion that is not as rapid as the expansion during phase 1. The duration of the phase Δt_4 is still a free parameter and its value is chosen to give the best-fitting spectral index. Finally, the value of τ_4 is calculated from the values of $C_{3\,4}$, b_4 and Δt_4 according to eqn (3.22). The best-fitting parameter values are listed in Table 4.7 and the resulting radio spectra are shown in Fig. 4.11.

As shown by the solid black curve in Fig. 4.11, this assumption of an expansion behind the shock front can fit the shape of the radio spectrum behind the shock front at all the measured frequencies. This scenario was investigated by finding the best-fitting values of the parameters that reproduce the flux density across all the measured frequencies. However, further modelling of the physical process which would cause the cocoon to expand after the shock passage is needed in order to be able to further investigate this scenario and whether it is plausible as a model.

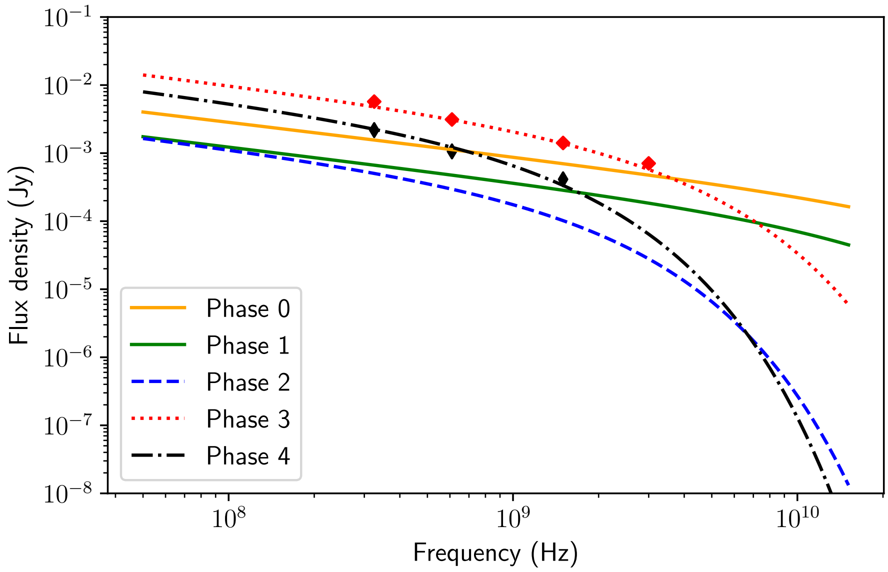

Figure 4.11: Flux densities from the modelling in scenario 4, where the radio cocoon continues to expand during the final phase of the model. All the phases of the model are shown. The measured flux densities at 80 kpc and 140 kpc are shown in the red and black point series, respectively.

Table 4.8: Comparison of the calculated spectral indices between 0.325 and 3.0 GHz at the end of each phase of the adiabatic model for the first four scenarios considered.

Phase	Spectral index			
	Case 1	Case 2	Case 3	Case 4
0	—	−0.535	−0.535	−0.535
1	—	−0.578	−0.578	−0.578
2	−1.35	−1.30	−1.30	−1.30
3	−1.03	−0.954	−0.954	−0.954
4	−1.58	−1.61	−2.32	−1.60

4.4 The effect of anisotropic emission with a weaker shock wave

In the calculations of the luminosity and the flux density in sections 4.3.1-4.3.4 above, it has been assumed that the emission pattern of the relic is isotropic. However, due to the compression caused by the shock passage, the magnetic field lines within the radio cocoon become significantly flattened. The degree of radio polarization of the emission should then depend on the angle between the plane of the shock and the line of sight (Laing, 1980). According to Enßlin & Gopal-Krishna (2001)[1], the luminosity should also depend on this angle, leading to an anisotropic emission pattern.

The value of the shock Mach number that was used in the modelling above is $\mathcal{M} = 1.7$. Although this value is somewhat smaller than the value $\mathcal{M} = 1.9$ which Van Weeren et al. (2017) found using the DSA-type re-acceleration model, a recent determination of the shock Mach number using new *Chandra* X-ray observations gave the result $\mathcal{M} = 1.13$ with a 90% upper confidence limit of $\mathcal{M} < 1.6$ (Andrade-Santos et al., 2019).

This section investigates applying the adiabatic model to the radio relic using a smaller shock Mach number, according to the recent findings, with an approximation of the effect of the anisotropic emission pattern. The first subsection looks at estimating the value of the boosting factor by which the luminosity and flux density is increased as a result of the anisotropic emission, while the second subsection looks at the application of the adiabatic scenario to the relic using a weak shock with a Mach number of $\mathcal{M} = 1.13$ and where the luminosity and flux densities at and behind the shock front are boosted by the factor found in the first section.

4.4.1 Estimate of the boosting factor

As a first approximation, the synchrotron power is related to the magnetic field according to

$$P_{\rm sync} \propto B_{\perp}^{(1-\alpha)}, \tag{4.5}$$

where $B_{\perp}$ is the component of the magnetic field that is perpendicular to the line of sight and α is the radio spectral index (Rybicki & Lightman, 1979).

For an isotropic distribution of the magnetic field lines, the magnetic field can be written as $B_{\perp} = B \sin\theta$, where θ is the angle between the direction of the

[1] Enßlin & Gopal-Krishna (2001) cite Enßlin et al. (1998) in support of this statement. However, Enßlin et al. (1998) only discuss the dependence of the radio polarization on the viewing angle and do not give any description of how the luminosity depends on the viewing angle.

magnetic field and the line of sight. Then the resulting luminosity (power) is obtained by taking the average of eqn (4.5) over all the possible angles:

$$P_{\text{sync}} \propto \left\langle (B \sin\theta)^{(1-\alpha)} \right\rangle = \frac{1}{\pi} \int_0^{\pi} B^{(1-\alpha)} (\sin\theta)^{(1-\alpha)} \mathrm{d}\theta. \tag{4.6}$$

On the other hand, if the magnetic field is perpendicular to the line of sight, then $B_\perp = B$ and the synchrotron power is simply given by eqn (4.5).

The factor by which the luminosity is expected to increase if the magnetic field is perpendicular to the line of sight is estimated to be the ratio of the luminosity for a perpendicular magnetic field to the luminosity of an isotropic magnetic field:

$$\text{Boosting factor} = \frac{P_{\text{sync}\,\perp}}{P_{\text{sync iso}}} = \frac{B^{(1-\alpha)}}{\left\langle (B \sin\theta)^{(1-\alpha)} \right\rangle}. \tag{4.7}$$

For a Mach number of $\mathcal{M} = 1.13$, the magnetic field value at and behind the shock front resulting from the adiabatic model is $B = 1.74\ \mu$G. Then for the value of the spectral index at the shock front, $\alpha = -0.95$, the boosting factor is calculated to be ~ 6. Similarly, behind the shock front the spectral index is $\alpha = -1.65$ which results in a boosting factor of ~ 7.

Since the anisotropic effect arises as a result of the compression by the shock front, it is probable that the magnetic field behind the shock front will start to become more isotropic and the boosting factor could decrease. For the purposes of this investigation, it is assumed that the boosting factor behind the shock front is the same as that at the shock front.

4.4.2 Scenario 5: Investigation of the adiabatic model with a smaller shock Mach number

This scenario extends scenario 2 from section 4.3.2 by using a value of $\mathcal{M} = 1.13$ and attempting to recover the flux density at the shock front using the boosting factor. The same initial electron spectrum was used as in scenario 2. Since the shock strength changed, the new value of the compression ratio of phase 3 was calculated to be $C_{2\,3} = 1.25$. To find the best-fitting values of the spectral indices at the end of phase 3 and 4, the durations of these phases were reduced so that $\Delta t_3 = 0.1$ Myr and $\Delta t_4 = 20$ Myr. The resulting value of τ_3 was -0.948 Myr. All the other phase parameters were kept the same as in scenario 2. The values of the phase parameters and the resulting magnetic field values and characteristic momenta are listed in Table 4.10. The resulting radio spectra are shown in Fig. 4.12.

As shown by the dotted red and dashed blue curves in Fig. 4.12, in the lower frequency region, the difference between the flux densities at the end of phase

Table 4.9: Best-fitting values of the phase parameters used in scenario 5 and the calculated cumulative compression ratios, magnetic field values, magnetic energy densities and characteristic momenta. The columns are grouped according to the phase parameters and the quantities that are calculated from the phase parameters.

Phase	Δt_i Myr	τ_i Myr	$C_{i-1\,i}$	b_i	$C_{0\,i}$	B_i μG	$u_{\mathrm{B}\,i}$ eV cm^{-3}	$p_{*0\,i}$
0	0	15.0	1	1.8	1.0	1.90	0.0899	∞
1	3.46	10.0	0.7	1.2	0.70	1.50	0.0559	303 000
2	54	∞	1	0	0.70	1.50	0.0559	22 100
3	0.10	-0.948	1.25	2	0.875	1.74	0.0752	22 00
4	20	∞	1	0	0.875	1.74	0.0752	15 900

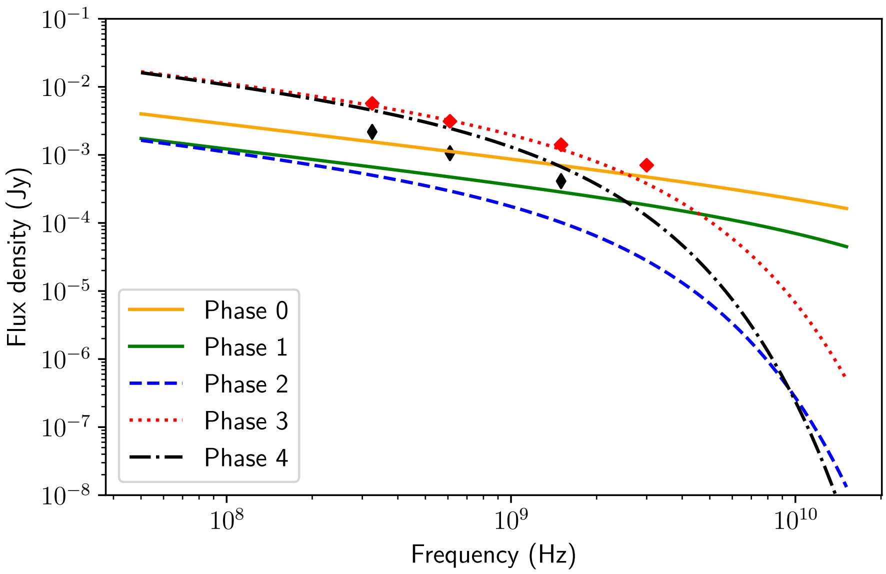

Figure 4.12: Flux densities from the modelling in scenario 5, where the electron population was injected by the radio galaxy and the emission at and behind the shock front is boosted as a result of the anisotropic magnetic field. All the phases in the model are shown.

Table 4.10: Calculated spectral indices at the end of each phase in scenario 5.

Phase	Spectral index
0	-0.535
1	-0.578
2	-1.30
3	-1.19
4	-1.61

2 and the end of phase 3 is slightly greater compared to scenario 2. This effect is a result of the boosting of the flux density at the shock front. Even though this scenario is based on a smaller shock Mach number, the flux density at the shock front is still recovered through the boosting factor. The radio spectrum at the end of phase 3 is slightly steeper than in scenario 2 and reducing the duration of phase 3 further did not change the spectral index significantly. There is, therefore, still a need to investigate the other factors such as the initial electron spectrum that will affect the shape of the radio spectrum at the shock front.

The estimate of the boosting factor in this scenario assumed that the magnetic field was perpendicular to the line of sight. However, the orientation of the magnetic field lines caused by the compression might not be complete and the direction of the shock motion could also not be perpendicular to the line of sight. Thus, this estimate should be taken as an upper limit. More detailed observations of the polarization properties of this relic, together with a comprehensive model of how the viewing angle can be estimated from the polarization would enable the angle between the magnetic field and the line of sight to be more accurately estimated, resulting in a better estimate of the boosting factor. Furthermore, this model of the boosting factor is only a first approximation and a more accurate model of how the luminosity of the relic depends on the viewing angle is needed to determine whether this scenario can recover the flux density of the relic.

Finally, as in scenario 2, the flux density at the end of phase 4 is still greater than the measured flux densities, indicating that the other mechanisms discussed in scenarios 3 and 4 are still necessary.

This scenario demonstrates that the boosting factor can still recover the flux density with a lower shock Mach number. However, further work is needed to reproduce the spectral index at the shock position using the weaker shock value. Since this scenario attempts to incorporate both the smaller Mach number that was recently determined and the compression of the magnetic field lines by the shock wave, this scenario provides a more complete understanding of the formation of the relic than the previous scenarios. Further observations of the polarization properties of the relic as well as comprehensive modelling of the viewing angle's dependence on the polarization and the dependence of the luminosity on the viewing angle, should enable a more accurate description of the relic formation to be produced.

4.5 General discussion

The previous two sections dealt with five scenarios in which the adiabatic model was applied to the radio relic hosted in A3411-3412 and presented the results of each of these scenarios together with a discussion in each case. This section discusses some of the more general implications found in the application of the adiabatic model.

The scenarios that dealt with the application of the full adiabatic model show that the emission of the galaxy, which is represented by the emission at the end of phase 0, starts to dominate at frequencies greater than 3.0 GHz. Thus, high frequency observations of the galaxy-relic system could enable this scenario of the relic formation to be tested more thoroughly.

As shown by these scenarios, the adiabatic model was able to reproduce the spectral index using a smaller Mach number than that found using the DSA-type re-acceleration model. Furthermore, the last scenario demonstrates that even for the smaller shock Mach number that was recently published, the adiabatic model is still successful if the boosting factor due to the compression of the magnetic field is taken into account. It has been found that, for small Mach numbers, the Mach number determined by the DSA model tends to be greater than the Mach number determined from the X-ray observations (Akamatsu et al., 2017; Colafrancesco et al., 2017) indicating that DSA models are not able to produce the observed flatness of the radio spectrum at the observed shock strength (Colafrancesco et al., 2017). The recent determination of the Mach number would seem to confirm this discrepancy in the case of this cluster. Since the adiabatic model is able to reproduce the observed spectrum with a smaller shock strength compared to the DSA-type re-acceleration model, it is a promising model for the formation of the radio relic in this cluster. Further modelling, taking into account the recent X-ray results, is needed to confirm whether the adiabatic model can describe the relic formation.

4.6 Conclusion

This chapter looked at the application of the adiabatic compression scenario to the north-eastern component of the radio relic that is hosted in the merging galaxy cluster A3411-3412. In the modelling a shock strength of $\mathcal{M} = 1.7$ was used and the free model parameters were chosen so that the spectral index at the end of each phase matched the spectral index at several points across the relic. Five different scenarios of the application of the model were studied. The first scenario took the electron spectrum at the end of the radio tail as the known electron spectrum at the end of phase 2 and followed the evolution of the spectrum from this point on. The next three scenarios took the electron spectrum of the radio galaxy as the electron spectrum of the injected electron population at the end of phase 0 and followed the evolution through all phases of the model. These scenarios differed from each other in the assumptions made on the fourth phase. The first of these scenarios attempted to match the spectral index and flux density at 140 kpc without any additional assumptions on phase 4. The second of these scenarios attempted to match just the flux density at 140 kpc and allowed the spectral index to be steeper than the measured spectral index at 140 kpc. The last of these scenarios, again, attempted to match both the flux density and the spectral index at 140 kpc by allowing the radio cocoon to expand during phase 4. The final scenario studied the effect of a weaker shock with $\mathcal{M} = 1.13$ and used the expected boosting factor to recover the flux density at the shock front.

The first four sets of results were able to reproduce the shape of the radio spectrum at the shock front. Furthermore, in scenarios 1, 2, and 4 the shape of the radio spectrum behind the shock front could also be reproduced, however, in scenarios 1 and 2 this also resulted in a flux density that was greater than the observed flux. Scenario 3 was able to reproduce the measured flux density at the lower frequencies using a longer duration for the final phase, although this resulted in a steeper spectrum that was not able to fit the point at the highest frequency. The fourth scenario reproduced both the spectral shape and the flux density behind the shock by allowing the radio cocoon to expand during the fourth phase. This could indicate that other mechanisms such as turbulence are active behind the shock front or that an expansion of the cocoon occurs during phase 4. Further modelling of such a scenario is needed in order to investigate what mechanisms could be effective behind the shock front.

These results show that the adiabatic compression scenario can reproduce the observed flat spectrum of the radio relic in the cluster A3411-3412. Moreover, these results were produced using a value of the shock strength that was smaller than the value predicted by the DSA-type re-acceleration model. This indicates that the adiabatic model could be more successful than DSA-type models in describing the origin of radio relics where the associated cluster shock is weak.

The comparison of the calculated flux densities to the measured flux densities is somewhat inconclusive for several reasons. Firstly, the normalization constant of the electron spectrum of the radio galaxy was only estimated based on the peak flux density of the relic. Further observations of the galaxy, particularly obtaining measurements of the flux density of the galaxy and the magnetic field within the galaxy, are needed to determine this constant more accurately. Secondly, the calculation of the flux density assumed that the emission is isotropic which is probably not the case. This anisotropic effect was studied briefly in scenario 5 but needs to be investigated further by describing more accurately how the luminosity depends on the viewing angle, which can be estimated from the level of polarization. Improving the accuracy of the calculated flux density would allow the adiabatic compression scenario to be tested more rigorously.

Finally, a further test of this scenario is to observe the galaxy-relic system at higher frequencies (greater than 3.0 GHz). The results of the modelling using all the phases of the compression scenario show that the emission at the end of phase 0 is predicted to dominate at these higher frequencies. Thus, high-frequency observations could test this prediction.

Chapter 5

Conclusion

This project has focused on the adiabatic compression model as a possible model for the origin of radio relics. In particular, the adiabatic model was applied to the radio relic hosted in the merging galaxy cluster Abell 3411-3412 in an attempt to reproduce the spectral index across the relic.

5.1 Summary

Chapter 2 presented the formalism of synchrotron radiation. The radio emission of relics is mainly due to synchrotron radiation and the formalism presented in this chapter was used throughout this work. Secondly, the expected spectral index due to synchrotron losses of the radio tail was calculated in order to confirm that synchrotron losses could explain the observed radiation in this region. Lastly, the normalization of the electron population was also calculated, as this spectrum was used later in chapter 4.

Chapter 3 presented the formalism of the adiabatic compression model and demonstrated that it could be extended to act on a generalized electron spectrum. Furthermore, the effect of the shock strength on the resulting radio spectrum was investigated and it was found that even for weak shocks the emission drops by only 2 orders of magnitude over the frequency range used. Lastly, the effect of the phase durations on the radio spectra at and behind the shock front was also investigated.

Chapter 4 applied the adiabatic compression model to the radio relic hosted in A3411-3412. Firstly, the spectral indices at various points across the relic that would correspond to the phases of the adiabatic model were chosen from the available observed values. The model was then applied to the relic in a simplified form by taking the electron spectrum at the end of phase 2 to be given by the electron spectrum at the end of the radio tail and the evolution of the spectrum was followed from this point on. This way of applying the model gave good results that reproduced the spectral index at the shock front. The full model was then applied to an electron spectrum that was taken to be a good approximation of the galaxy electron spectrum. These results were also promising and were able to reproduce the spectral index at the shock front. However, it was also found that the spectral index and flux density behind the shock front could not be so easily reproduced. This could indicate that there are other mechanisms that take place in this region. One such mechanism, an expansion phase behind the shock front, was investigated and did seem to be able to reproduce both the flux density and the spectral index. Another mechanism that could affect the evolution of the electron spectrum is turbulence behind the shock front. Lastly, the adiabatic model was applied to the relic but a smaller Mach number of the shock was assumed and the possible effect of an anisotropic emission pattern was briefly investigated.

5.2 Future work on the relic hosted in A3411-3412

This project shows that the adiabatic compression model can be extended to act on a generalized electron spectrum and that even for low Mach number shocks, emission that has a spectral index comparable to the typical spectral index of relics is still produced. Furthermore, the adiabatic model is able to reproduce the spectral index of the relic in A3411-3412 at the position of the shock front using a Mach number that is smaller than the Mach number predicted in the DSA-type re-acceleration model.

In this work, the boosting factor was introduced in order to try to model the effect of an anisotropic magnetic field on the luminosity and resulting flux density. A partial alignment of the magnetic field is expected as a result of the compression caused by the shock wave (Laing, 1980; Enßlin & Gopal-Krishna, 2001). It is necessary to be able to model the effect this alignment has on the luminosity in order to calculate the expected flux density accurately. The model presented in this work is very rough, and further modelling of this effect is needed.

In future work, further modelling of the relic at a lower shock Mach number, taking into account the effect of the anisotropic emission, is also needed to confirm the advantage that the adiabatic compression model may have over the DSA-type models. Further work is also needed to describe and model other mechanisms that could possibly take place behind the shock front.

In order to further test this application of the adiabatic model, more observations of the galaxy-relic system are needed. Observations that provide more accurate detail of the magnetic field and flux density of the galaxy are needed to be able to deduce the electron spectrum of the injected radio plasma. Furthermore, observations that provide a better understanding of the structure of the relic and the flux densities and spectral indices across the relic are needed for a comparison with the fluxes predicted by the adiabatic model. Finally, since the adiabatic model predicts that the galaxy emission should start to dominate at frequencies greater than 3 GHz, observations of the galaxy-relic system at higher frequencies could test the predictions of the adiabatic compression model. MeerKAT and the upcoming SKA will be very important for such observations given their sensitivity and angular resolution that should allow for the detection of the radio emission, as well as the measurement of the spectrum at several frequencies, even in low-brightness regions such as the end of the radio tail.

5.3 Future work to test the adiabatic compression model as a common mechanism for the origin of relics

Although the DSA model is widely used to describe the origin of relics, it is inefficient at low shock Mach numbers and in several clusters there is a discrepancy between the Mach number predicted within the DSA model and the Mach number determined from X-ray observations (Akamatsu et al., 2017; Colafrancesco et al., 2017). This could indicate that the DSA model can only be applied to relics where the associated cluster shock wave is fairly strong, and that for relics where the associated cluster shock wave is weak an alternative model for the origin of the relic is needed.

The results of this work seem to indicate that the adiabatic compression scenario can be more successful in describing the origin of relics where the associated shock wave is weak. Since the durations of the dormant phase and the compression phase can be greater than those used in this project, this model can be used even for moderate shocks, as in the scenarios described by Enßlin & Gopal-Krishna (2001). This model does require that there is a source of fossil electrons which would require that a radio galaxy is connected to the relic. Such a connection has also been found in other clusters (e.g. PLCKG287.0+32.9 Bonafede et al., 2014, and the Bullet cluster Shimwell et al., 2015) which suggests that this could be a common origin for radio relics. Furthermore, the success of the adiabatic model in reproducing the spectral index of this relic could indicate that sources categorized as radio gischt, as well as sources categorized as radio phoenices, could be produced through adiabatic compression, which seems to suggest that there is no real distinction between these two classes of sources.

This model would not be efficient if an undetectable cool gas is present in the plasma. In this case the shock wave should penetrate the plasma allowing the electrons to be energized via DSA. However, there will still be adiabatic gains, although these will be limited due to the small compression factor (Enßlin & Gopal-Krishna, 2001).

References

Akamatsu H., et al., 2017, Astronomy and Astrophysics, 600, A100

Alexander P., Leahy J., 1987, Monthly Notices of the Royal Astronomical Society, 225, 1

Allen S. W., Evrard A. E., Mantz A. B., 2011, Annual Review of Astronomy and Astrophysics, 49, 409

Andrade-Santos F., et al., 2019, The Astrophysical Journal, 887, 31

Arnaud M., Evrard A. E., 1999, Monthly Notices of the Royal Astronomical Society, 305, 631

Bagchi J., Enßlin T., Miniati F., Stalin C., Singh M., Raychaudhury S., Humeshkar N., 2002, New Astronomy, 7, 249

Begelman M., Cioffi D., 1989, The Astrophysical Journal, 345, L21

Blandford R., Eichler D., 1987, Physics Reports, 154, 1

Blumenthal G. R., Faber S. M., Primack J. R., Rees M. J., 1984, Nature, 311, 517

Bonafede A., Intema H., Brüggen M., Girardi M., Nonino M., Kantharia N., van Weeren R., Rottgering H., 2014, The Astrophysical Journal, 785, 1

Bosma A., 1981, Astronomical Journal, 86, 1825

Brüggen M., Bykov A., Ryu D., Röttgering H., 2012, Space Science Reviews, 166, 187

Colafrancesco S., Marchegiani P., Paulo C. M., 2017, Monthly Notices of the Royal Astronomical Society, 471, 4747

Colless M., et al., 2001, Monthly Notices of the Royal Astronomical Society, 328, 1039

De Gasperin F., et al., 2017, Astronomy and Astrophysics, 597, A15

Di Gennaro G., et al., 2018, The Astrophysical Journal, 865, 24

Dicke R., Peebles P., Roll P., Wilkinson D., 1965, The Astrophysical Journal, 142, 414

Drury L. O., 1983, Reports on Progress in Physics, 46, 973

Enßlin T. A., Gopal-Krishna 2001, Astronomy and Astrophysics, 366, 26

Enßlin T. A., Biermann P., Klein U., Kohle S., 1998, Astronomy and Astrophysics, 332, 395

Feretti L., Giovannini G., Govoni F., Murgia M., 2012, Astronomy and Astrophysics Review, 20, 54

Ferrari C., et al., 2015, in Advancing Astrophysics with the Square Kilometre Array (AASKA14). p. 75 (`arXiv:1412.5801`)

Ferrière K. M., 2001, Reviews of Modern Physics, 73, 1031

Fixsen D. J., Cheng E. S., Gales J. M., Mather J. C., Shafer R. A., Wright E. L., 1996, The Astrophysical Journal, 473, 576

Fujita Y., Takizawa M., Yamazaki R., Akamatsu H., Ohno H., 2015, The Astrophysical Journal, 815, 116

Geller M. J., Huchra J. P., 1989, Science, 246, 897

Gendron-Marsolais M., Hlavacek-Larrondo J., van Weeren R., Clarke T. Fabian A., Intema H., Taylor G., Blundell K., Sanders J., 2017, Monthly Notices of the Royal Astronomical Society, 469, 3872

Ghosh S., Jain P., Kashyap G., Kothari R., Nadkarni-Ghosh S., Tiwari P., 2016, Journal of Astrophysics and Astronomy, 37, 25

Giovannini G., Vacca V., Girardi M., Feretti L., Govoni F., Murgia M., 2013, Monthly Notices of the Royal Astronomical Society, 435, 518

Goss W., McAdam W., Wellington K., Eckers R., 1987, Monthly Notices of the Royal Astronomical Society, 226, 979

Harrison E. R., 1970, Phys. Rev. D, 1, 2726

Hawkins S., Ellis G. F. R., 1965, Physics Letters, 17, 246

Hinshaw G., et al., 2013, The Astrophysical Journal Supplement Series, 208, 19

Hubble E., 1929, Proceedings of the Natural Academy of Sciences, 15, 168

Jaffe W., Perola G., 1973, Astronomy and Astrophysics, 26, 423

Jones C., Forman W., 1999, The Astrophysical Journal, 511, 65

Kaiser C., Alexander P., 1997, Monthly Notices of the Royal Astronomical Society, 286, 215

Kaiser C., Dennett-Thorpe J., Alexander P., 1997, Monthly Notices of the Royal Astronomical Society, 292, 723

Kang H., Ryu D., Cen R., Ostriker J., 2007, The Astrophysical Journal, 669, 729

Kang H., Ryu D., Jones T. W., 2012, The Astrophysical Journal, 756, 97

Kempner J., Blanton E., Clarke T., Enßlin T., Johnston-Hollitt M., Rudnik L., 2004, in Proceedings of the Riddle of Cooling Flows in Galaxies and Clusters of Galaxies. Charlottesville, VA, pp 335–339

Kravtsov A. V., Borgani S., 2012, Annual Review of Astronomy and Astrophysics, 50, 353

Laing R., 1980, Monthly Notices of the Royal Astronomical Society, 193, 439

Landau L., Lifshitz E., 1959, Fluid mechanics. Course on Theoretical Physics, Pergamon Press, Oxford

Longair M. S., 2011, High Energy Astrophysics, 3rd edn. Cambridge University Press, Cambridge

Macario G., et al., 2014, Astronomy and Astrophysics, 565, A13

Markevitch M., Vikhlinin A., 2007, Physics Reports, 443, 1

Mather J. C., et al., 1990, Astrophysical Journal Letters, 354, L37

Mitchell R. J., Culhane J. L., Davison P. J. N., Ives J. C., 1976, Monthly Notices of the Royal Astronomical Society, 175, 29P

Ogrean G., Brüggen M., van Weeren R., Röttgering H., Simionescu A., Hoeft M., J.H. C., 2014, Monthly Notices of the Royal Astronomical Society, 440, 3416

Ostriker J. P., Peebles P. J. E., 1973, The Astrophysical Journal, 186, 467

Pearce C. J. J., et al., 2017, The Astrophysical Journal, 845, 81

Peebles P. J. E., Yu J. T., 1970, The Astrophysical Journal, 162, 815

Penzias A., Wilson R., 1965, The Astrophysical Journal, 142, 419

Perlmutter S., et al., 1999, The Astrophysical Journal, 517, 565

Pfrommer C., Springel V., Enßlin T. A., Jubelgas M., 2006, Monthly Notices of the Royal Astronomical Society, 367, 113

Pinzke A., Oh S., Pfrommer C., 2013, Monthly Notices of the Royal Astronomical Society, 435, 1061

Press W. H., Schechter P., 1974, The Astrophysical Journal, 187, 425

Rajpurohit K., et al., 2018, The Astrophysical Journal, 852, 65

Roettiger K., Stone J. M., Burns J. O., 1999, The Astrophysical Journal, 518, 594

Rybicki G. B., Lightman A. P., 1979, Radiative Processes in Astrophysics. Wiley, New York, NY

Ryu D., Kang H., Hallman E., Jones T. W., 2003, The Astrophysical Journal, 593, 599

Sanderson A., Ponman T., Finoguenov A., Lloyd-Davies E., Markevitch M., 2003, Monthly Notices of the Royal Astronomical Society, 340, 989

Sarazin C. L., 1988, X-ray Emission from Clusters of Galaxies. Cambridge Astrophysics Series, Cambridge University Press, Cambridge

Schlickeiser R., 2002, Cosmmic Ray Astrophysics. Astronomy and Astrophysics Library, Springer-Verlag, Berlin

Shimwell T., Markevitch M., Brown S., Feretti L., Gaensler B., Johnston-Hollitt M., Lage C., Srinivasan R., 2015, Monthly Notices of the Royal Astronomical Society, 449, 1486

Shu F., 1992, Gas Dynamics. The Physics of Astrophysics Vol. 2, Univeristy Science Books, Sausalito, CA

Trimble V., 1987, Annual Review of Astronomy and Astrophysics, 25, 425

Van Weeren R., Röttgering H., Brüggen M., Hoeft M., 2010, Science, 330, 347

Van Weeren R. J., Röttgering H. J. A., Intema H. T., Rudnick L., Brüggen M., Hoeft M., Oonk J. B. R., 2012, Astronomy and Astrophysics, 546, A124

Van Weeren R., et al., 2013, The Astrophysical Journal, 769, 101

Van Weeren R., Andrade-Santos F., Dawson W., Golovich N., Lal D., Kang H., Ryu D., 2017, Nature Astronomy, 1, 0005

Van Weeren R., de Gasperin F., Akamatsu H., Brüggen M., Feretti L., Kang H., Stroe A., Zandanel F., 2019, Space Science Review, 215, 16

Vazza F., Brüggen M., 2014, Monthly Notices of the Royal Astronomical Society, 437, 2291

Vazza F., Eckert D., Brüggen M., Huber B., 2015, Monthly Notices of the Royal Astronomical Society, 451, 2198

Vikhlinin A., Kravtsov A., Forman W., Jones C., Markevitch M., Murray S. S., Speybroeck L. V., 2006, The Astrophysical Journal, 640, 691

Voit G. M., 2005, Reviews of Modern Physics, 77, 207

White D. A., Fabian A. C., 1995, Monthly Notices of the Royal Astronomical Society, 273, 72

Wilber A., et al., 2018, Monthly Notices of the Royal Astronomical Society, 473, 3536

Wilson T. L., Matteucci F., 1992, The Astronomy and Astrophysics Review, 4, 1

Wright E., 2006, Publications of the Astronomical Society of the Pacific, 118, 1711

Zhang C., Churazov E., Forman W. R., Lyskova N., 2019, Monthly Notices of the Royal Astronomical Society, 488, 5259

Zwicky F., 1937, The Astrophysical Journal, 86, 217